



# Shallow cavity flow tone experiments: onset of locked-on states

D. Rockwell<sup>a,\*</sup>, J.-C. Lin<sup>a</sup>, P. Oshkai<sup>a</sup>, M. Reiss<sup>a</sup>, M. Pollack<sup>b</sup>

<sup>a</sup>Department of Mechanical Engineering and Mechanics, 354 Packard Laboratory, 19 Memorial Drive West, Bethlehem, PA 18015, USA

<sup>b</sup>Lockheed-Martin, USA

Received 15 May 2001; accepted 19 September 2002

## Abstract

Fully turbulent inflow past a shallow cavity is investigated for the configuration of an axisymmetric cavity mounted in a pipe. Emphasis is on conditions giving rise to coherent oscillations, which can lead to locked-on states of flow tones in the pipe–cavity system. Unsteady surface pressure measurements are interpreted using three-dimensional representations of amplitude–frequency, and velocity; these representations are constructed for a range of cavity depth. Assessment of these data involves a variety of approaches. Evaluation of pressure gradients on plan views of the three-dimensional representations allows extraction of the frequencies of the instability (Strouhal) modes of the cavity oscillation. These frequency components are correlated with traditional models originally formulated for cavities in a free-stream. In addition, they are normalized using two length scales: inflow boundary-layer thickness and pipe diameter. These scales are consistent with those employed for the hydrodynamic instability of the separated shear layer, and are linked to the large-scale mode of the shear layer oscillation, which occurs at relatively long cavity length. In fact, a simple scaling based on pipe diameter can correlate the frequencies of the dominant peaks over a range of cavity depth.

The foregoing considerations provide evidence that pronounced flow tones can be generated from a fully turbulent inflow at very low Mach number, including the limiting case of fully developed turbulent flow in a pipe. These tones can arise even for the extreme case of a cavity having a length over an order of magnitude longer than its depth. Suppression of tones is generally achieved if the cavity is sufficiently shallow.

© 2003 Elsevier Science Ltd. All rights reserved.

## 1. Introduction

A conceptual framework for the generation of flow tones requires, first of all, consideration of strictly hydrodynamic oscillations in an acoustic-free system, then the coupling of such oscillations with the acoustic mode(s) of a resonator. These concepts, as well as related issues and objectives are described below.

### 1.1. Cavity oscillations in an acoustic-free system

The origin, or stimulus, of locked-on flow tones is the inherent, organized unsteadiness of the velocity and vorticity fields along the cavity. Fig. 1a shows the essential features of self-sustaining cavity oscillations: (a) vorticity concentration(s) incident upon the trailing corner of the cavity; (b) upstream influence of the vorticity distortion at the trailing corner to the sensitive region of the shear layer formed from the leading corner of the cavity; (c) conversion of the upstream disturbance arriving at the leading-edge to a fluctuation in the separating shear layer; and (d) amplification of this fluctuation in the shear layer as it develops in the streamwise direction. To be sure, for the case of

\*Corresponding author. Tel.: +1-610-758-4107; fax: +1-610-758-4041.

E-mail address: dor0@lehigh.edu (D. Rockwell).

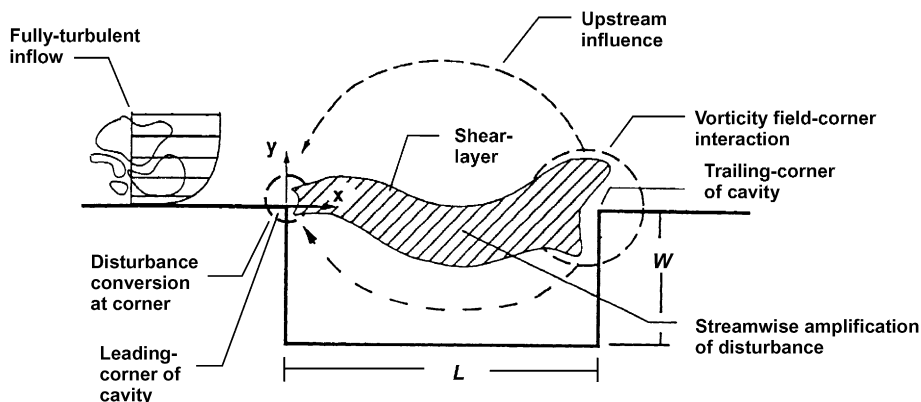


Fig. 1. Principal elements of self-sustaining oscillation of turbulent flow past cavity associated with purely hydrodynamic effects.

fully turbulent inflow, organized unsteadiness of the shear layer along the cavity may not be immediately evident; nevertheless, the shear layer may exhibit a predisposition for broadband undulations. The basic elements associated with self-sustained oscillations described in Fig. 1a were defined in the early investigation of Powell (1961) for the simpler case of a planar jet impinging upon a leading-edge. Since then, Rockwell and Naudascher (1978, 1979); Rockwell (1983), Blake (1986), Howe (1997), and Rockwell (1998) have described these elements for a variety of configurations of impinging shear layers, including the cavity configuration.

## 1.2. Cavity oscillations in an acoustic-resonant system

Flow past a cavity in presence of an acoustic resonator, such as a long pipe, can exhibit coupling with one or more resonant modes of the pipe. This type of lock-on has conceptual similarities to that occurring in a wide variety of other flow-acoustic configurations. Rockwell and Naudascher (1978, 1979); Rockwell (1983, 1998) and Blake (1986) summarize extensive investigations of locked-on oscillations due to flow past cavity configurations, including not only quasi-two-dimensional geometries, but also circular, triangular, and whistle-shaped cavities. Representative systems that exhibit lock-on behavior are described below.

### 1.2.1. Jet excitation of a long organ pipe

Large amplitude oscillations of the jet at the mouth of an organ pipe occur during resonant coupling with a pipe mode(s). Cremer and Ising (1967, 1968) visualize the jet oscillations and analyze the jet-organ pipe as a controlled system. Techniques for determining the amplitude and phase of the controller are also addressed. This same class of resonant coupling is reviewed by Fletcher (1979), who describes further aspects of the jet-organ pipe configuration from a systems perspective. Moreover, further aspects of nonlinear interactions in organ flue pipes are analyzed in works summarized by Fletcher (1979).

### 1.2.2. Jet-sequential orifice plates

Resonant coupling of the jet instability through a series of orifice plates, i.e., baffles, simulates the coupling that occurs in segmented solid rocket motors. In this case, the acoustic wavelength is the same order, or less than, the baffle spacing. In other words, the resonator is the cavity. Flatau and Van Moorham (1990) emphasize the importance of distinguishing between the resonance of inlet and nozzle cavities, relative to resonance of the total test-section. Further insight into this type of lock-on configuration is provided by Hourigan et al. (1990). They employ a discrete vortex simulation, in conjunction with the theoretical concept of Howe (1975, 1980), to assess the generation of instantaneous acoustic power. A recent investigation of locked-on flow tone generation in a baffle system by Stoubos et al. (1999) emphasizes the empirically determined amplitude and frequency response characteristics of the tone as a function of flow velocity through the baffle system. All of the foregoing investigations are, in certain respects, related to early experiments on the fluid mechanics of whistling undertaken by Wilson et al. (1971). In their work, a set of two sequential orifice plates, each having rounded edges, gives rise to well-defined whistles or tones, and the nature of the jet instability related to these types of flow tones is similar to those of the foregoing studies.

### 1.2.3. Wake from a flat plate in a test-section

Vortex shedding from the blunt trailing-edge of a flat plate in the test-section of a wind tunnel gives rise to highly coherent resonant coupling with the acoustic mode(s) of the plate–test-section system. These modes are often referred to as Parker modes, based on the investigations of [Parker \(1966\)](#), which are summarized by [Cumpsty and Whitehead \(1971\)](#). The latter provide a theory that allows the amplitude of the forced acoustic mode to be predicted from the pressure field below resonance and the measured damping factor of the acoustic mode. [Stoneman et al. \(1988\)](#) have recently undertaken an additional, in-depth investigation of a similar lock-on phenomena involving two plates in tandem in a duct.

### 1.2.4. Cavity shear layer–cavity resonator

For the case of an orifice in a wall bounded by a closed cavity, [DeMetz and Farabee \(1977\)](#) determined the response characteristics of the coupled shear layer–cavity resonance as a function of the character of the inflow boundary layer, i.e., whether it is laminar or turbulent. [Elder \(1978\)](#) provides a systems model in conjunction with measurements. [Elder et al. \(1982\)](#) give detailed spectra and mode characterization of flow tone generation due to both laminar and turbulent boundary layers approaching the cavity. Moreover, a model is formulated for the self-excited oscillations. [Nelson et al. \(1981, 1983\)](#) have undertaken detailed measurements of the time-averaged unsteady shear layer in relation to the overall response characteristics of the coupled system. In their more recent study, momentum and energy balances are employed to characterize the physics of these oscillations.

### 1.2.5. Cavity shear layer–side branch duct/pipe

Early characterization of the frequency and amplitude characteristics in a jet-pipe (side branch) resonator was undertaken by [Pollack \(1980\)](#). Coupled resonant oscillations that occur in a pipe branch system have been addressed both theoretically and experimentally by [Bruggeman et al. \(1989, 1991\)](#) and [Kriesels et al. \(1995\)](#). In essence, this configuration represents the flow past a deep cavity. Both experiments and theory are employed to explain the acoustic and hydrodynamic conditions for resonance. This analysis leads to a concept that provides the ratio of acoustic to steady flow amplitudes. [Ziada and Buehlmann \(1992\)](#) and [Ziada and Shine \(1999\)](#) characterize this class of coupling for various side branch configurations.

### 1.2.6. Cavity shear layer–long pipeline

The radiated sound due to lock-on of oscillations due to flow past a cavity inserted in a long pipeline has been experimentally characterized in a series of investigations extending from [Davies \(1981\)](#) to [Davies \(1996a,b\)](#). Sound propagation within, and radiation from, various configurations is summarized therein. The primary emphasis of these investigations has been identification of the locked-on resonant frequencies, rather than an understanding of the underlying physics. [Rockwell and Schachenmann \(1982, 1983\)](#) provided the first measurements of the physical behavior of the unsteady shear layer along the mouth of a circular cavity at the end of a long pipe, in conjunction with the locked-on and nonlocked-on states. Concepts of linearized, inviscid stability theory were employed as a guide to determining the phase shifts and amplitude spikes across the shear layer. In addition, they characterized the streamwise phase difference, which is essential to the locked-on condition. Moreover, they also showed that during lock-on, the magnitude of the fluctuating velocity due to acoustic resonance can be of the same order as that associated with the hydrodynamic (vorticity) fluctuations. This coexistence of acoustic and instability waves can give rise to false standing wave patterns along the core of the jet in an acoustically resonant system, as emphasized by [Rockwell and Schachenmann \(1980\)](#). Such false, short wavelength patterns are not limited to locked-on, self-excited cavity oscillations. They also occur in acoustically forced jets, as described by [Pfizenmaier \(1973\)](#).

Further insight into the lock-on phenomena that occur in the cavity–pipeline system is provided by [Rockwell and Karadogan \(1982\)](#). Using zero-crossing statistics, in conjunction with recursive digital filtering, they determined the self- and cross-probability density of velocity and pressure. The degree of phase fluctuation of organized oscillations of turbulent jet flow through the cavity was characterized in terms of a mean phase deviation from the locked-on condition. In this manner, it is possible to characterize phase fluctuations as the phase-locked condition is approached.

Finally, attenuation of pipeline–cavity oscillations has been undertaken by [Rockwell and Karadogan \(1983\)](#). A variety of attenuation configurations were considered. Among them, small-scale vortex generators were shown to be very effective in attenuating the lock-on oscillations.

### 1.3. Cavity oscillations in an acoustic–resonant pipe system: unresolved issues and objectives

Very little is known of self-excited oscillations of a fully turbulent inflow past a cavity, which is bounded on either side by a pipe. Coherent oscillations are expected to occur when an acoustic resonant mode of the pipe–cavity system is compatible with an inherent instability of the turbulent shear layer past the cavity. The major unresolved issues are:

- (a) The possibility of locked-on flow tones arising from a fully turbulent inflow and, in the limiting case, of a fully developed turbulent flow in a pipe, has not been clarified. The onset of such flow tones would require growth of an inviscid instability on the turbulent background of the separated shear layer past the cavity.
- (b) Flow tones in relatively shallow cavities at very low values of Mach number have not been addressed. More specifically, when the acoustic wavelength is much longer than the length of the cavity, then acoustic resonance cannot occur within the cavity. Most investigations of flow tones at low Mach number have involved sufficiently deep cavities, such that the large-scale instability of the separated shear layer develops in a relatively unhindered fashion. As the cavity becomes relatively shallow, it is anticipated that the growth of large-scale vortical structures is hindered, and conditions for the onset of shear layer–resonator coupling, leading to flow tones, may not be attainable.
- (c) The appropriate dimensionless scaling for the frequencies of dominant pressure amplitude peaks of flow tones, provided they exist, has not been established. It is expected that, for a relatively deep cavity, which is sufficiently long such that the large-scale vortical structures develop, scaling based on pipe diameter  $D$  would be appropriate. In this case, it is anticipated that the vortical structures would correspond to the fully developed axisymmetric instability of the jet-like shear layer through the cavity. The possibility of extending this type of scaling to extremely shallow cavities has not been addressed. Furthermore, the sensitivity of this scaling based on diameter  $D$  to variations in the inflow boundary layer thickness has not been clarified. If the large-scale instability evolves to the same form along a relatively long cavity, irrespective of the initial boundary layer thickness, the case for scaling of the dimensionless frequency based on  $D$  would be even more compelling.
- (d) The manner in which the amplitudes of flow tones are attenuated as a function of depth of a shallow cavity is unknown. Furthermore, the possibility of the nonexistence of flow tones at a very small cavity depth is an important limit that has not been defined. A further, important aspect is whether discernible spectral peaks, which would represent a low-level instability in absence of flow tone generation, can be detected in very shallow cavities.
- (e) The effect of mode spacing of the resonant modes of the pipe–cavity system, as well as the absolute frequency of the lowest mode of the pipe–cavity system, may influence the types of transformation between the resonant modes of the pipe–cavity system when the inflow velocity is altered. This feature has not been addressed for either deep or shallow cavity–pipe configurations.

The objectives of the present investigation are centered on these unresolved issues. Pressure measurement techniques will be employed in conjunction with the three-dimensional images of the pressure amplitude response and techniques for assessing these images.

## 2. Experimental system and techniques

### 2.1. Overview of experimental system

The experimental system was designed and manufactured in the Fluid Mechanics Laboratories at Lehigh University. In essence, the system consists of two principal subsystems. The first is the air supply system, and the second is the actual pipeline–cavity system. These two subsystems are located in different rooms, with a thick ceramic wall between them, in order to isolate mechanical vibrations associated with the compressor system.

### 2.2. Air supply system

The air supply system involves an air compressor, which provides air to a compressed air plenum. Within the compressed air plenum, the air is maintained at a gauge pressure of 552–689 kPa (80–100 psig). The air exhausts from the plenum into an air dryer where water is separated from the air. A filter system extracts undesirable particles from the air. The air is then transmitted through the isolation wall into the room housing the main experimental facility.

An overview of the pipeline–cavity system is given in Fig. 2a. A pipe–valve arrangement for regulating low and high flow rates to the pipeline–cavity system is located at its upstream end. When low velocities through the pipeline–cavity

system are desired, air is sent through a series of two pressure regulators to accurately control the flow rate. The first regulator operates at high pressures and takes the air input from approximately 621 kPa gauge (90 psig) to 138 kPa gauge (20 psig). The second regulator then limits the air output to a maximum of approximately 14 kPa gauge (2 psig), which corresponds roughly to a maximum of 9.1 m/s (30 ft/s) through the pipe. When it is desired to generate higher velocities through the pipeline–cavity system, the second regulator, which operates at lower pressures, is bypassed. In this case, the maximum centerline velocity through the pipe system is approximately 61 m/s (200 ft/s). In summary, the role of this pipe–valve system is to provide a regulated, constant air supply to the inlet plenum of the main pipeline–cavity system, as indicated in Fig. 2a.

### 2.3. Pipeline–cavity system

#### 2.3.1. Inlet plenum

The inlet plenum of the pipeline–cavity system is shown in the plan and side views of Fig. 2a. It is constructed from Plexiglas, and houses a 2.5-in thick layer of honeycomb, which acts as a flow straightener. Moreover, the inside of the plenum is lined with acoustic damping foam to minimize local acoustic resonances. The exit of the plenum is attached to a contraction, which was designed to prevent localized separation in the pipe inlet. To ensure that the large changes in pressure gradient near the exit of the nozzle did not produce localized perturbations that would propagate downstream and, furthermore, to generate a fully turbulent boundary layer, a trip ring was located immediately downstream of the exit of the plenum contraction. This ring was located at a distance of 35 mm from the pipe inlet. It had a thickness of 1 mm, and was 4 mm long. Its geometry involved a series of adjacent triangular cuts along the leading-edge of the ring.

#### 2.3.2. Pipeline–cavity arrangement

The main pipeline–cavity arrangement was located downstream of the inlet plenum, as indicated in Fig. 2a. The first version of this system, shown in Fig. 2a, consists of two 2.4 m (8 ft) segments of 25.4 mm (1 in) ID aluminum piping, located on the upstream and downstream sides of the Plexiglas cavity. This aluminum pipe had a thickness of 3.2 mm. A total of three pressure transducers were located in the inlet (upstream) pipe. They were positioned at distances of 127, 1213, and 2365 mm upstream of the exit of the inlet (upstream) pipe. Furthermore, a similar system of transducers was mounted on the exhaust (downstream) pipe. They were located at distances of 78 and 1218 mm upstream of the exit of the pipe.

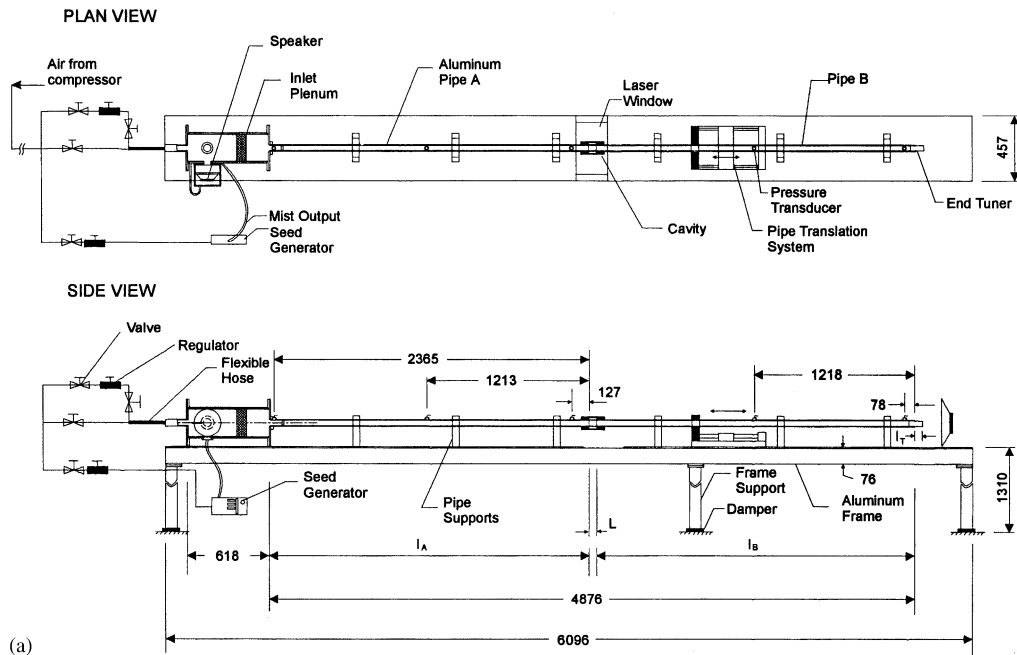


Fig. 2. (a) Overview of pipeline–cavity system. (b) Details of cavity subsystem.

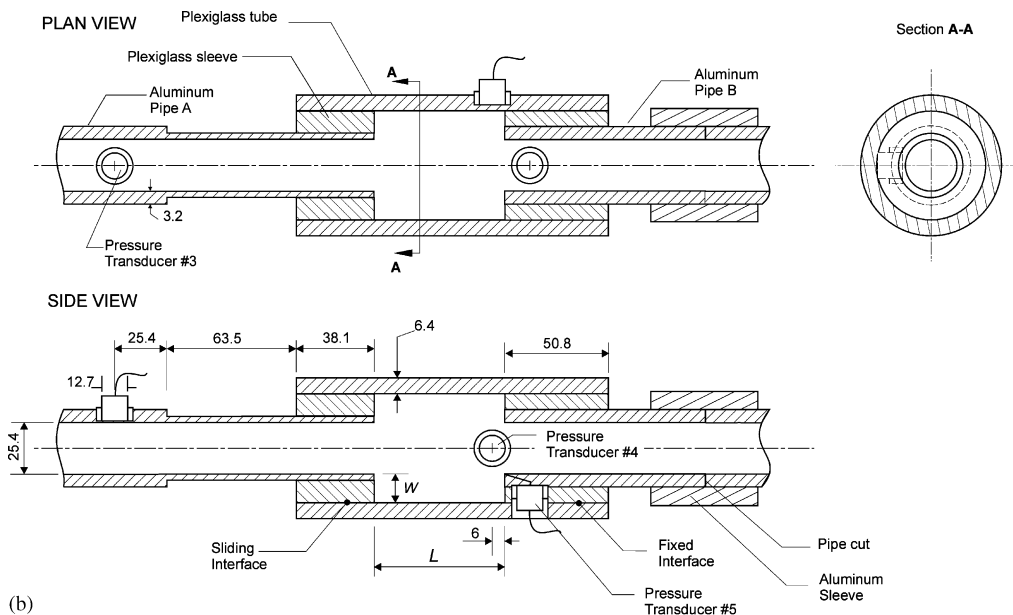


Fig. 2 (continued).

The second version of the pipeline–cavity system employed the same inlet plenum and cavity; however, shorter inlet (upstream) and exhaust (downstream) pipe sections were employed. These sections had a length of 30.48 cm (12 in). One pressure transducer was located in the inlet (upstream) pipe at a distance of 125 mm from the pipe exit. Regarding the exhaust (downstream) pipe, one transducer was also mounted along this pipe at a distance of 152 mm from the pipe exit.

The mode numbers  $N$  of the aforementioned pipeline–cavity systems were determined from broadband loudspeaker excitation. By examination of the spectra of the pressure response and use of the relation  $f_N = Nc/2L_T$ , in which  $L_T$  is the total length of the pipeline–cavity system, it was possible to relate the mode  $N$  to each peak in the pressure spectrum. For the results presented herein, the long-pipe–cavity system showed self-excited modes extending from  $N = 12$  to 22, which corresponds to values of frequency  $f_N = 410$ –750. Similarly, for the short-pipe–cavity system, modes  $N = 2$ –6 were excited, corresponding to values of frequency  $f_N = 550$ –1650. For both the long- and short-pipeline–cavity systems, only even-numbered modes  $N$  were self-excited. If it is viewed that the inlet pipe A and outlet pipe B are excited independently, the mode number  $N$  is replaced by  $2N$ .

The effective damping of the pipeline–cavity systems was determined in the absence of mean flow using loudspeaker excitation. Two approaches were employed. The first recorded the transient decay of the pressure amplitude as a function of time, following abrupt termination of loudspeaker excitation. In this case,  $Q = n_0\pi$ , in which  $n_0$  is the number of cycles required to decay to  $1/e$  of the initial pressure amplitude. The second approach involved band-limited white noise excitation, which yielded the power spectral density of the pressure response. In this case, the quality  $Q$ -factor of the resonant acoustic mode is  $Q = \omega_0/(\omega_2 - \omega_1)$ , where  $\omega_0$  is the center frequency, and  $\omega_1$  and  $\omega_2$  are the half-power points on the lower and upper sides of the spectral peak. Generally, similar values of  $Q$ -factor, taking into account experimental uncertainty, were obtained for the transient decay and band-limited point noise excitation techniques. More extensive data were acquired using the latter approach, and the best fit through these data for the long-pipeline–cavity system shows values of  $Q = 70$ –100 for mode numbers  $N = 12$ –22. For the short-pipeline–cavity system, the values of  $Q$  were predominantly in the range  $Q = 70$ –120 for mode numbers  $N = 2$ –4. The uncertainties that arise during evaluation of the  $Q$ -factor are primarily due to the finite resolution in the frequency domain, which is linked to the values of the frequencies  $\omega_0$ ,  $\omega_1$ , and  $\omega_2$ . The uncertainties of  $Q$  are estimated to be approximately 20%, using the equation of Kline and McClintock (1953).

### 2.3.3. Mounting arrangement for pressure transducers

The pressure transducers located along the inlet (upstream) and exhaust (downstream) pipes were PCB high sensitivity transducers (Model U103AO2); the same transducers were employed for measurements within the cavity

system, as described subsequently in Section 2.4. Each pressure transducer was mounted to be as flush as possible to the interior surface of the pipe. This was accomplished using the technique of Peters (1993). The diameter of the sensing hole in the pipe wall was 2.5 mm and its depth was 0.25 mm. This mounting arrangement ensures, for the range of frequencies of interest in this investigation, that no acoustic resonant effects were generated in the region between the face of the transducer and the surface of the pressure tap at the interior of the pipe.

#### 2.4. Cavity subsystem

The cavity system is shown in Fig. 2b. The inlet (upstream) aluminum pipe, designated as pipe A, is maintained in a fixed position on the pipe supports. The left end of the Plexiglas tube slides along the exterior of a smoothly machined exterior surface of the inlet (upstream) pipe A. In essence, this sliding arrangement allows adjustment of the cavity length  $L$  with a high degree of accuracy and repeatability. This adjustment was achieved by employing a traverse mechanism (see the pipe translation system in Fig. 2a), which translated the entire pipe B and the Plexiglas tube attached to it. The junction between the interior of the Plexiglas tube and the exterior of the exhaust (downstream) aluminum pipe B is fixed. The internal diameter  $D$  of the two pipes A and B is 25.4 mm (1 in).

The downstream end of pipe A and the upstream end of pipe B form the leading- and trailing-edges of the cavity, respectively. In order to obtain different values of cavity depth  $W$ , the exterior diameters of pipes A and B were altered. This was accomplished by placing Plexiglas sleeves around the ends of pipes A and B. Correspondingly, the interior diameter of the Plexiglas tube was altered as well. Since it was desired to investigate a total of four values of cavity depth  $W^* = W/D = 1.25, 0.5, 0.25$  and  $0.125$ , in which  $D = 25.4$  mm (1 in) this meant that four different aluminum pipe–Plexiglas-tube combinations were manufactured.

Pressure transducers were deployed in order to obtain pressure measurements on the trailing- (impingement-) corner of the cavity, as well as on the floor of the cavity. In subsequent notations of pressure measurements, the pressure transducer in the pipe upstream of the cavity is designated as  $p_3$ , that at the corner as  $p_5$ , and that on the cavity floor as  $p_4$  (see Fig. 2b). Since both of these transducers ( $p_4$  and  $p_5$ ) were fixed with respect to pipe B and the Plexiglas tube attached to it, their position, relative to the trailing-corner of the cavity, remained unaltered when the cavity length  $L$  was varied. Unless otherwise indicated, all measurements herein correspond to pressure transducer  $P_3$ .

#### 2.5. Pressure measurements

##### 2.5.1. Pressure transducers

PCB transducers (Model No. U103A02) were employed for pressure measurement. These transducers have a nominal sensitivity of 1727 mV/psi. The outputs from the transducers were connected to a PCB Piezotronics multi-channel signal conditioner, Model 48A. This multi-channel conditioner allowed independent adjustment of the gains of the pressure transducer signals. Generally speaking, however, it was possible to employ the same value of gain for all pressure measurements. This gain adjustment is important in order to meet the required voltage input levels of the A/D (analog/digital) board.

##### 2.5.2. Acquisition of pressure signals

The conditioned pressure signals were transmitted to ports on a National Instruments board (Model PCI-MI0-16E-4) with 12-bit resolution. This board, when operating in the single-channel acquisition mode, can sample at the rate of 250KS/s, in which  $K = 10^3$  and  $S$  is the number of samples. In the present scenario, a total of eight pressure transducers were employed, so the effective sampling rate is reduced by a factor of eight, i.e., it takes on a value of 31KS/s per channel. In essence, there are two considerations to determine whether this sampling rate is adequate. First of all, for characterization of pressure in the frequency domain, the sampling rate should be at least twice the maximum frequency of interest. For representations in the time domain, a minimum of five samples per cycle is required, but a minimum of 10 samples per cycle is desirable. Considering these requirements together, the acquisition system should have a sampling rate at least 10 times as high as the maximum typical frequency of interest in the present investigation, which corresponds approximately to  $1.5 \times 10^3$  Hz. This requirement is approximately a factor of 20 lower than the acquisition rate of 31KS/s per channel. It is also important to realize that this type of board basically consists of one A/D (analog/digital) converter, and the acquisition of eight pressure signals is accomplished using a multiplexing technique. The scan interval is defined as the time required to go from a recorded point corresponding to pressure transducer No. 1, through the sequence of the other seven transducers, and return to the channel of transducer No. 1. This scan interval is basically the inverse of the maximum data acquisition rate per channel is  $1/(31.25 \times 10^3)$ , which corresponds approximately to 32  $\mu$ s.

### 2.5.3. Processing of pressure signals

A Pentium II 350 MHz computer and LabView software were used to process the pressure transducer signals. The major parameters for spectral analysis using the fast Fourier transform (FFT) must be properly defined so that adequate resolution in the frequency domain is accomplished, while at the same time minimizing the amount of collected data. In order to determine which values of each parameter were adequate, a series of averaging tests were performed using broadband noise input. For a given set of parameters, the number of averaged files was varied to determine the minimum number of files and, hence, the minimum number of data samples needed to properly represent the system response.

The parameters were: (i) the number of samples acquired per data set; (ii) the sampling rate; and (iii) the number of data sets employed to obtain an average. The sampling rate must be twice as high as the maximum frequency of interest. Therefore, the necessary sampling rate varied directly with the maximum frequency of interest for each experiment. The value of the frequency resolution ( $\Delta f$ ) is equal to the sampling rate ( $f_s$ ) divided by the number of samples per data set ( $n_s$ ). Once the sampling rate was determined for each experiment, the number of samples was calculated according to  $n_s = f_s/\Delta f$ .

In order to determine the value for  $\Delta f$ , another set of averaging experiments was performed. Values of  $\Delta f$  were varied. These tests showed that  $\Delta f = 0.5$  Hz adequately characterized the system response, while providing acceptable frequency resolution at both the low and high ends of the frequency range of interest in this research program. At the lowest and highest frequencies of interest, approximately 35 and 1500 Hz,  $\Delta f/f$  has its maximum and minimum values of 0.014 and 0.00034, respectively.

During acquisition of final experimental data, the sampling rate was set to 4096 samples per second, which resulted in a Nyquist frequency of 2048 Hz, well above the maximum frequency component of interest for this research, which was approximately 1500 Hz. The number of samples per data set ( $n_s$ ) was then specified, while maintaining  $\Delta f = 0.5$  Hz, resulting in  $2^{13} = 8192$  samples per data set. Each of the spectra represented herein was obtained by averaging a total of 42 data sets. According to Newland (1993), the accuracy  $\sigma/m$  can be estimated using the relationship  $\sigma/m \cong 1/\sqrt{B_e T}$  in which  $\sigma$  and  $m$  are the standard deviation in the mean value of the measurement, respectively,  $B_e$  is the effective bandwidth of the spectral window and  $T$  is the record length. Using the effective value of record length  $T$ , this results in a value of  $\sigma/m = 0.154$ . In the assessment of Newland (1993), it is indicated that values of  $\sigma/m = \frac{1}{3}$  are generally acceptable. Furthermore, the convergence of the calculated spectra as a function of the number of averaged spectra was undertaken using the band-limited white noise technique of loudspeaker excitation as described in Section 2.3. This process was employed for a number of selected resonant modes of both the long-pipeline- and short-pipeline-cavity systems. For example, excitation of mode  $N = 16$  for the long-pipeline-cavity system, i.e., for band-limited white noise centered at mode  $N = 16$ , as few as 10 averages yielded a peak amplitude at  $N = 16$  that was indistinguishable from the value determined from a larger number of averages, up to a total of 100 averages, within an uncertainty of 5%.

Unless otherwise indicated, all pressure measurements herein correspond to a reference location (i.e., at pressure transducer  $p_3$  as defined in Section 2.4) in the pipe resonator. Comparisons of measurements at different locations are given in Section 6.

### 2.6. Velocity measurements

In order to characterize in detail the mean and fluctuating velocity distributions at the exit of the inlet (upstream) pipe A, hot wire anemometry was employed. A miniature hot wire probe was traversed across the pipe exit. The traverse system was equipped with a linear variable displacement transducer (LVDT), so that the position of the hot wire probe could be positioned with a precision of approximately 0.1 mm. In-house software was used to calculate the mean and fluctuating velocity components from the raw hot-wire signal.

For the wide range of measurements during the course of this investigation, it was necessary to have an accurate and repeatable means to determine the time-averaged centerline velocity  $\bar{u}_m$ . This was accomplished by using a pressure tap on the side of the inlet plenum and a tap located at the exit of the orifice plate, which was attached to the downstream end of the plenum. The difference between these two pressure measurements provided a reference value for calculating the centerline velocity of the flow through the pipe. This pressure difference was calibrated against the centerline velocity at the exit of the exhaust (downstream) pipe B using two different approaches. The first involved the calibrated hot wire, described in the above, and the second was based on the measurement of total pressure by means of a Pitot probe at the exit of the pipe. The total pressure was measured using one of the two Validyne transducers, model DP103-104, for smaller values of flow velocity and model DP15-24 for higher values of flow velocity.

### 3. Inflow conditions

A major purpose of the present investigation is to determine whether self-excited flow tones can be generated when the inflow conditions are fully turbulent. Proper specification of the inflow conditions is important in several respects. First of all, it is desirable to ensure that quasi-laminar or transitional phenomena do not exist in the approach flow. For the limiting case of laminar inflow, i.e., a laminar boundary layer, self-excited coherent oscillations, which have pronounced spectral peaks, can be generated even in the absence of a coexisting acoustic resonance of the cavity or an adjacent pipe.

A second reason for specifying details of the inflow conditions is to facilitate the scaling of the dimensionless frequencies of oscillation. Geometric parameters are often used to characterize the frequency of oscillation, e.g.,  $fL/U$ , in which  $L$  is the cavity length and  $U$  is the characteristic velocity or  $fD/U$ , where  $D$  is the diameter of the inflow pipe. Such geometric scaling does not account for the variations of boundary layer thickness that exist in different practical configurations.

The momentum thickness  $\theta = \int_0^\infty (\bar{u}/\bar{u}_m)(1 - \bar{u}/\bar{u}_m) dy$  is typically employed to represent the characteristic thickness of a shear flow. In this investigation, velocity  $\bar{u}$  is the average streamwise velocity at any location, and  $\bar{u}_m$  is its value at the centerline of the pipe. The value of  $\theta$  was determined for the extreme cases of velocity distributions described in this section. The distributions of mean and fluctuating velocity are considered for two basic cases: (a) a long pipe, having a length to diameter ratio of 96, which ensures a fully developed flow at the pipe exit; and (b) a relatively short pipe having a length to diameter ratio of 12, which has a turbulent boundary layer at its exit that is not fully developed. As indicated in Section 2, a boundary layer trip ring was located at the pipe inlet for both cases of the long and short pipes. This trip promotes the rapid onset of turbulence, which was especially important for the case of the short pipe.

Prior to characterizing the values of momentum thickness for the long and short inlet pipes, efforts were focused on ascertaining the turbulent nature of the flow at the exit of each pipe. This involved determination of distributions of normalized root-mean-square velocity  $u_{rms}$  across the pipe. These distributions were found to be in agreement with established results. In addition, the logarithmic form of the velocity distribution was pursued. The traditional semi-logarithmic representation of the mean velocity distribution at the exit of the long pipe was verified.

Distributions of dimensionless mean velocity  $\bar{u}/\bar{u}_m$  as a function of dimensionless distance  $y/R$  from the pipe wall are exhibited in Fig. 3 for the short (top plot) and long (bottom plot) inlet pipes. Considering first of all the distributions of mean velocity given at the top of Fig. 3, a relatively flat region exists from approximately  $y/R = 0.4-1.0$ , corresponding to the “core” region of the pipe flow. Data for the velocities  $70.7 \leq \bar{u}_m \leq 131.5$  are remarkably coincident. For these velocity distributions, the dimensionless momentum thickness falls in the range of  $0.029 \leq \theta_0/R \leq 0.035$ . The definition of  $\theta_0 = \int_{y=0}^{y=R} (\bar{u}/\bar{u}_m)(1 - \bar{u}/\bar{u}_m) dy$  was employed.

The bottom plot of Fig. 3 represents the corresponding velocity distribution for the case of the long inlet pipe. The values of momentum thickness  $\theta_0$  normalized by the pipe radius  $R$  lie in the range  $0.088 \leq \theta_0/R \leq 0.096$ .

### 4. Overview of characteristics of pressure fluctuations

The nature of unsteady pressure fluctuations arising from flow past a shallow cavity is complicated by variations in the cavity depth. In contrast to the overwhelming share of previous investigations, where the cavity depth is much larger than the characteristic thickness of the inflow shear layer, the existence of a sufficiently shallow cavity is expected to substantially alter the onset and growth of instabilities in the separating shear layer. The consequence is a rich variety of possible flow states within the cavity. In the present investigation, emphasis is on the case of a sufficiently long cavity length  $L_m$  such that, for a deep cavity, the fully evolved axisymmetric instability of the separated shear layer occurs. This limiting case is well studied for the corresponding case of a free axisymmetric jet. In fact, as will be discussed, the scaled frequencies of a sufficiently deep cavity agree remarkably well with this limiting, reference case. Moreover, preliminary diagnostics showed that the largest amplitude spectral peaks occurred for this long cavity length  $L_m$ , irrespective of the cavity depth  $W$ . The present results provide extensive characterization of the unsteady pressures as a function of inflow velocity  $U$ , cavity depth  $W$ , and the thickness of the inflow shear layer.

#### 4.1. Summary of ranges of parameters

The cavity length was adjusted to a fixed value of  $L_m^* = L_m/D = 2.5$ , which, as indicated in the foregoing, allowed the fully evolved axisymmetric instability mode to develop in the deepest cavity. The cavity depth was then varied according to  $W^* = W/D = 1.25, 0.5, 0.25, \text{ and } 0.125$ . The largest value of depth  $W^* = 1.25$  should, in concept, represent a sufficiently deep cavity, such that the instability in the free shear layer develops in a relatively unhindered fashion. At

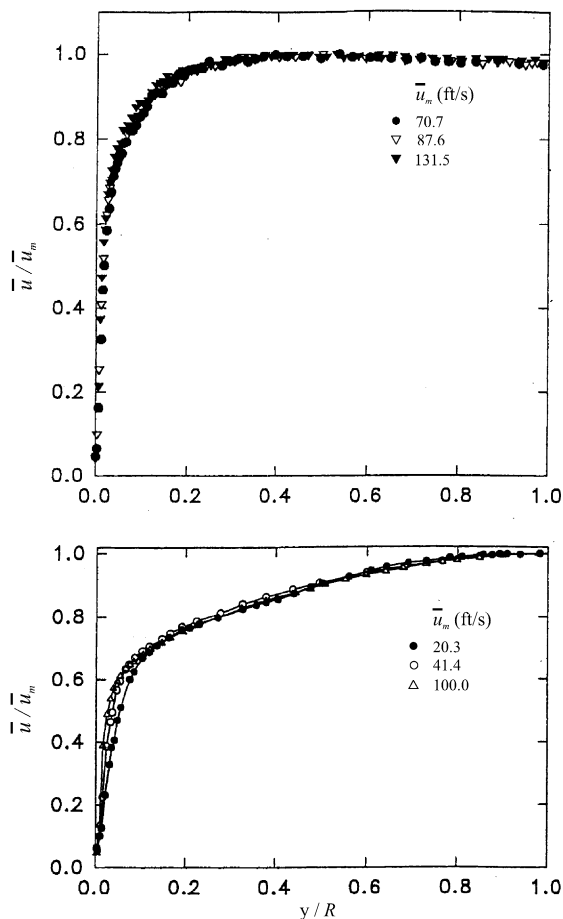


Fig. 3. Direct comparison of time-mean velocity variations across short inlet pipe (top plot) and long inlet pipe (bottom plot).

the other extreme,  $W^* = 0.125$  is small in comparison with the pipe diameter  $D$ , and thereby represents the case of a very shallow cavity. The inflow velocity  $U$  was varied up to a maximum value of approximately 200 ft/s, depending upon the particular experimental configuration. Furthermore, the characteristic thickness of the inflow boundary layer was altered by attaching both long and short inlet pipes; this approach led to extreme values of momentum thickness  $\theta_0$ , as described in Section 3.

#### 4.2. Methods of presentation of data

Features of the fluctuations are represented by pressure spectra. The pressure amplitude is averaged over the effective bandwidth  $\Delta f$  of the spectral analysis. For a given experimental run, a relatively large number of spectra are acquired. It is therefore useful to develop a unified, comprehensive presentation of families of spectra. This was accomplished by developing a color coded, isometric view; a representative image of this type is given in Fig. 4a. In constructing these representations, a total of 37–40 spectra were employed. In the case where velocity was varied during the experimental run, values of spectral amplitude were interpolated along the velocity axis. Similarly, for the case where the cavity length was altered, interpolation was carried out in the direction of the cavity length. The magnitudes of pressure were color (gray level) coded, such that gradations of color are evident in three-dimensional space, thereby providing an overview of the conditions for which relatively high-pressure amplitudes are generated. Since the focus of this program is on conditions for the onset of flow tones, most of the changes in color level are concentrated at lower values of pressure amplitude. Once a threshold value of amplitude is exceeded, the color magnitude is maintained the same for all higher values. This color was, in fact, white. As a consequence of this approach, it is not possible to determine, in certain cases, the maximum amplitude of the pressure spectra based on the three-dimensional color plots. Complete

families of spectra are therefore provided in a separate compendium, so that the reader can easily deduce details of each individual spectrum.

A plan view of each isometric, three-dimensional color (gray level) plot is also provided in each case. It allows a perspective on a plane of velocity versus frequency and identification of high values of pressure amplitude. This type of view also gives a rapid indication of the extent of each locked-on mode of a flow tone.

Further representations of the pressure variations involve either isometric or plan views of logarithmic, as opposed to linear, pressure amplitude. This type of view emphasizes the variation of the background fluctuations, in addition to the resonant values associated with generation of flow tones.

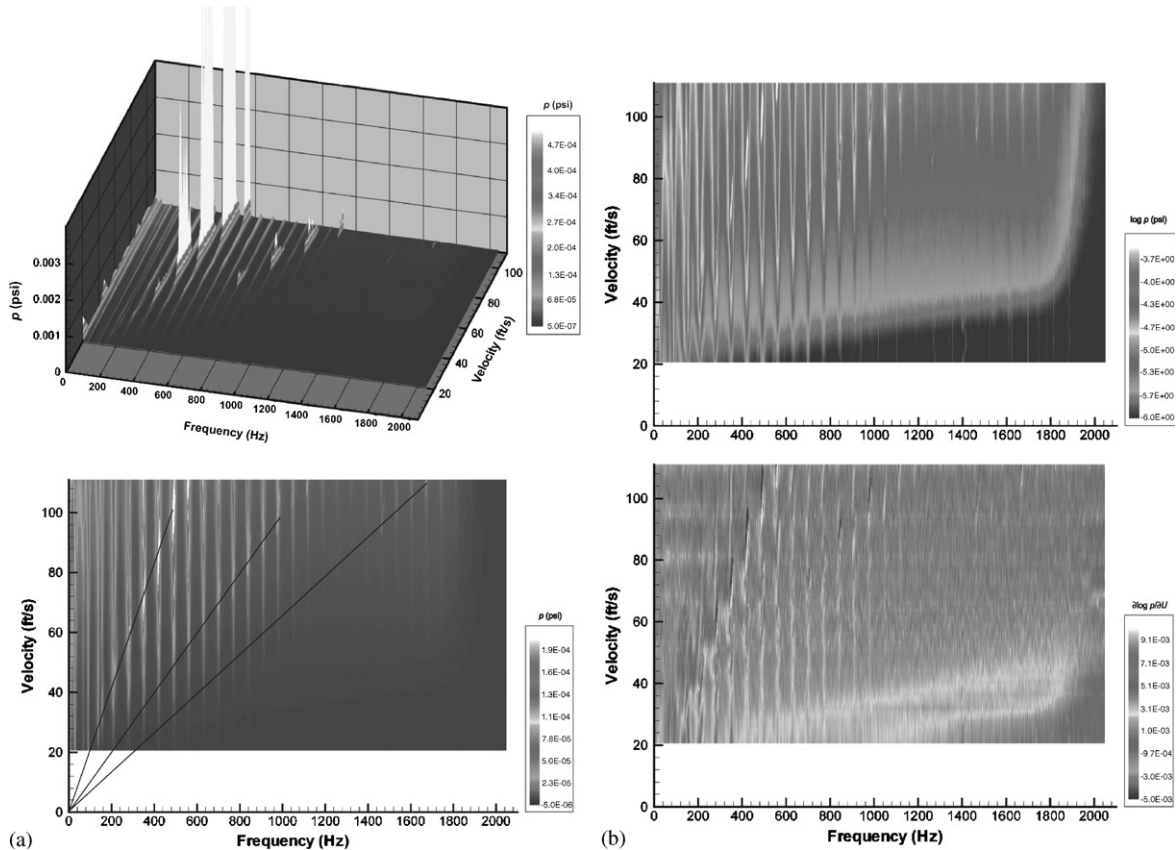


Fig. 4. (a) Isometric view (top image) and plan view (bottom image) of pressure amplitude as a function of frequency and velocity. Lines shown on plan view represent fits through peak values of pressure amplitude. Cavity length  $L^* = L/D = 2.5$  and depth  $W^* = W/D = 1.25$ , where  $D$  is pipe diameter. Long pipes of equal length are located at either end of the cavity. (b) Plan view of logarithmic pressure amplitude as a function of velocity and frequency (top image); and plan view of magnitude of the derivative of the logarithmic pressure amplitude with respect to velocity,  $\partial(\log p)/\partial U$  (bottom image). Cavity length  $L^* = L/D = 2.5$  and depth  $W^* = W/D = 1.25$ , where  $D$  is pipe diameter. (c) Isometric view (top image) and plan view (bottom image) of pressure amplitude as a function of frequency and velocity. Lines shown on plan view represent fits through peak values of pressure amplitude. Cavity length  $L^* = L/D = 2.5$  and depth  $W^* = W/D = 0.5$ , where  $D$  is pipe diameter. (d) Isometric view of logarithmic pressure amplitude as a function of velocity and frequency (top image); and plan view of magnitude of the derivative of the logarithmic pressure amplitude with respect to velocity,  $\partial(\log p)/\partial U$  (bottom image). Cavity length  $L^* = L/D = 2.5$  and depth  $W^* = W/D = 0.5$ , where  $D$  is pipe diameter. (e) Isometric view (top image) and plan view (bottom image) of pressure amplitude as a function of frequency and velocity. Lines shown on plan view represent fits through peak values of pressure amplitude. Cavity length  $L^* = L/D = 2.5$  and depth  $W^* = W/D = 0.25$ , where  $D$  is pipe diameter. (f) Isometric view (top image) and plan view (bottom image) of pressure amplitude as a function of frequency and velocity. Cavity length  $L^* = L/D = 2.5$  and depth  $W^* = W/D = 0.125$ , where  $D$  is pipe diameter. (g) Overview of effect of cavity depth on three-dimensional representation of pressure amplitude as a function of velocity and frequency. In all cases, cavity length is constant at  $L^* = L/D = 2.5$ . Cavity depth varies according to  $W^* = W/D = 1.25$  (top image),  $W^* = W/D = 0.25$  (middle image), and  $W^* = W/D = 0.125$  (bottom image).

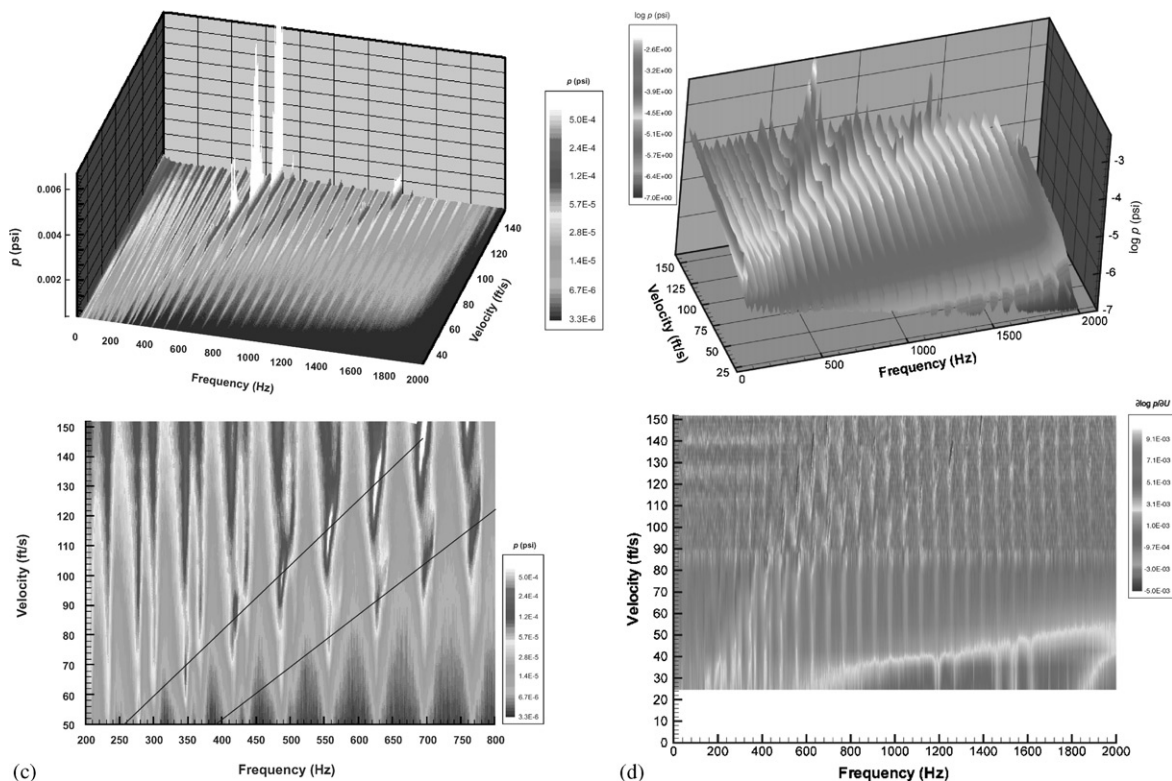


Fig. 4 (continued).

Finally, effort was devoted to implementing a means of detecting peaks in the plot of logarithmic pressure amplitude. The principal aim here was to educe low-level peaks of pressure, which otherwise remain undetected in simple plots of logarithmic pressure amplitude or linear pressure amplitude. Once these peaks were identified, they could be represented on the plane of velocity versus frequency, in order to determine the variation of the inherent instability frequency of the shear layer, i.e., Strouhal frequency, that gives rise to vortex formation. A successful approach to educing low level peaks involved, first of all, taking the derivative of the logarithmic pressure amplitude with respect to velocity. This derivative may be written as

$$\partial(\log p) / \partial U. \tag{4.1}$$

Once this derivative is evaluated, it is plotted in a color (gray level) coded form on either the velocity versus frequency plane or the velocity versus cavity length plane. The magnitudes of the derivatives are color coded in such a manner that a pressure peak, which corresponds to an essentially discontinuous change in the sign of the slope, according to Eq. (4.1), is represented by a sharp junction between two distinctive colors. A line passing through these detected peaks is then plotted on the aforementioned plan view of pressure amplitude as a function of velocity versus frequency or, alternately, on the plan view of pressure amplitude in relation to cavity length versus velocity. This is a very effective approach to identify a low amplitude peak that is not associated with a flow tone, but nevertheless represents a localized peak due to the inherent instability mode of the shear layer, which is accentuated by presence of the resonator.

In the following, the types of color representations described in the foregoing are shown, first of all, for (a) variations of the inflow velocity and (b) alterations of the cavity length  $L$ .

### 4.3. Pressure fluctuations for variations of inflow velocity

The pressure response characteristics of the pipeline–cavity that correspond to variations of inflow velocity are examined for the two extreme inflow shear layers defined in Section 3. As described therein, these different inflow conditions are generated via attachments of long and short inlet pipes.

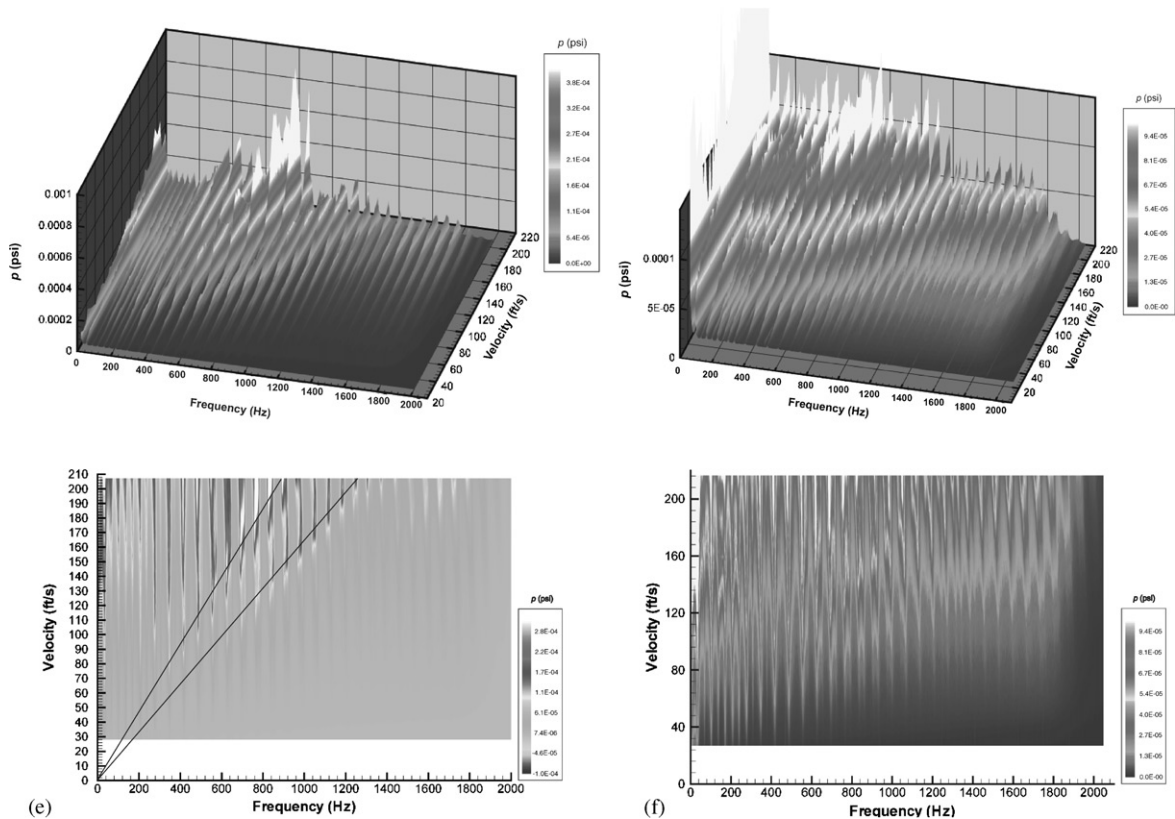


Fig. 4 (continued).

#### 4.3.1. Long inlet pipe–cavity system

Figs. 4a–f exhibit the pressure amplitude response that corresponds to variations of inflow velocity  $U \equiv \bar{u}_m$ , i.e., the averaged velocity at the centerline of the pipe. The cavity length  $L$  is maintained at its maximum value, designated as  $L_m$ . Variations of cavity depth  $W$  are considered. Figs. 4a and b show the case of a relatively deep cavity and, at the other extreme, Fig. 4f represents the shallowest cavity.

For the case of the deepest cavity exhibited in the top image of Fig. 4a, pronounced peaks of pressure amplitude are evident at values of inflow velocity of the order of 70 ft/s and higher. Harmonics of these peaks are either very small or indistinguishable. The peaks shown in this image coincide with the resonant modes of the long-pipe–cavity system having frequencies approximately in the range from 300 to 600 Hz. The bottom image of Fig. 4a, which shows a plan view of the variation of pressure amplitude over the plane of frequency versus inflow velocity  $U$ , indicates clearly the sequential excitation of higher modes of the resonant pipe–cavity system with increasing velocity. The thin, elongated white regions correspond to the peaks exhibited in the isometric view, i.e., in the top image of Fig. 4a. At the center of each of these peak (white) regions, the amplitude of the pressure in the neighboring resonant modes is small. On the other hand, near the edges of a given peak (white) region, there is clearly simultaneous excitation of two neighboring resonant modes. This feature is inherent to excitation of flow tones in resonant systems having multiple resonant modes. The black lines indicated in the bottom image of Fig. 4a represent constant values of dimensionless frequency  $fL/U$ . They pass through the pressure peaks. Although the line having the largest slope passes through distinct and highly visible peaks, the remaining two lines pass through peaks that are less well defined. In order to extract these peaks, the plan view corresponding to the bottom image of Fig. 4a was directly compared with the bottom image of Fig. 4b, which employs the criterion for identification of peaks.

The top image of Fig. 4b shows a plan view of the pressure amplitude on the velocity–frequency plane. It is based on the same data as Fig. 4a, except the pressure is expressed in terms of its logarithmic value, i.e.,  $\log p$ . This plot shows further features of locally high values of pressure amplitude outside the clearly distinct peaks. The bottom

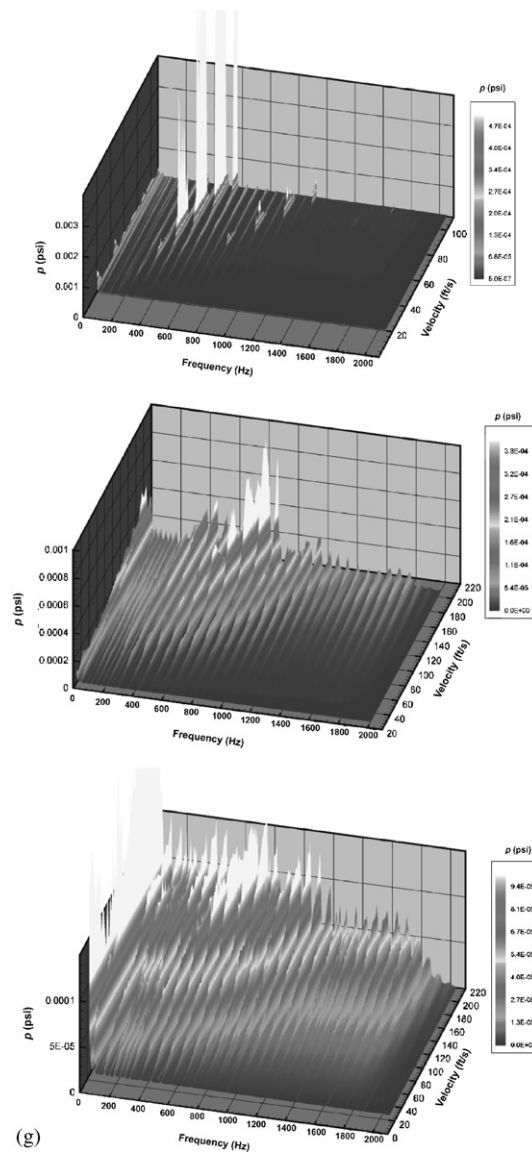


Fig. 4 (continued).

image of Fig. 4b is a plan view of the variation of the parameter  $\partial(\log p)/\partial U$  over the velocity versus frequency plane. As addressed in the foregoing, this parameter aids in peak identification. At locations of the peaks, the slopes on either side of the peak abruptly change from positive to negative values, and thereby the colors (gray level) show an abrupt change. It should be emphasized that this type of representation shown in the bottom image of Fig. 4b is simply intended to serve as an aid in extracting peaks. By no means does it provide an indication of lock-on associated with generation of flow tones. This concept of lock-on will be addressed subsequently.

Figs. 4c and d represent the case of a shallower cavity having a depth  $W^* = 0.5$ . The most striking feature of the top image of Fig. 4c, in comparison with the case of the deeper cavity corresponding to Fig. 4a, is that the velocity for onset of a pronounced peak is shifted to a higher value of approximately 120 ft/s, which is approximately 50% larger than the onset velocity for the deep cavity of Fig. 4a. Generally speaking, however, the overall form of the distribution of peaks is similar to that of Fig. 4a for the deep cavity. Observations of the bottom image of Fig. 4c are, in many respects,

similar to the corresponding plan view of Fig. 4a. Lines of constant  $fL/U$  are linear and pass through the sequence of pressure peaks. In Fig. 4d, the plot of logarithmic pressure amplitude is shown in an isometric view (top image), in order to further emphasize the locally large values of pressure amplitude, in addition to the well-defined peaks evident in Fig. 4c. This plot also clearly shows the increase in background pressure fluctuation amplitude as the velocity is increased. The plot of magnitude of  $\partial(\log p)/\partial U$  on the plane of velocity versus frequency, represented by the bottom image of Fig. 4d, is directly analogous to the corresponding plot of Fig. 4b.

A further decrease in cavity depth to a value of  $W^* = 0.25$  is represented in Fig. 4e. The top image of Fig. 4e shows the generation of a number of well-defined peaks, which are coincident with the resonant modes of the pipe-cavity system. An important observation is that these peaks are generated only at very high values of inflow velocity, i.e., of the order of  $U = 150$  ft/s and larger. Although there may be a tendency to interpret these peaks as an indication of locked-on flow tones, this may not be the case; further assessments are required and are addressed in Section 6. The plan view of linear pressure amplitude on the plane of velocity versus frequency is represented in the bottom image of Fig. 4e. The white regions, which indicate the highest amplitude peaks, generally do not have the same sharply defined symmetrical form as exhibited previously in the bottom images of Figs. 4a and c. Nevertheless, there is a tendency for these white, peak-like regions to follow a constant  $fL/U$ , i.e., the black line having the greatest slope in the bottom image of Fig. 4e. As in the previously described cases corresponding to deeper cavities, the black line of the lower slope was constructed with the aid of the pressure gradient concept defined by Eq. (4.1).

The case of the shallowest cavity,  $W^* = 0.125$ , is shown in Fig. 4f. The top image of Fig. 4f reveals that significant peaks are attainable only at the highest values of flow velocity of the order of  $U = 200$  ft/s. Since these peaks have very low amplitude, it is possible to observe an increase in pressure amplitude for all of the pipe-cavity modes as the inflow velocity increases. Considering the bottom image of Fig. 4f, which shows the plan view of linear pressure amplitude  $p$  on the plane of velocity versus frequency, it is clear that isolated, distinct pressure peaks cannot be defined in the same manner as for deeper cavities, i.e., in the bottom images of Figs. 4a–e. It is therefore not possible to construct lines of constant  $fL/U$ . This lack of a clearly defined Strouhal line of constant  $fL/U$  was further reaffirmed by examination of contours of constant pressure gradient calculated according to Eq. (4.1).

An overview of the pressure amplitude response for extreme values of cavity depth  $W$  is given in Fig. 4g. These three-dimensional images are taken from Figs. 4a, e, and f. The transformation from sharply defined pressure peaks to a larger number of less sharply defined peaks having much lower amplitude is clearly indicated for decreasing values of cavity depth. Further observations are as follows: shallower cavities require a higher value of minimum flow velocity to attain a locked-on flow tone; for a sufficiently small cavity depth, lock-on is not attainable; and, for deeper cavities, lower order resonant modes lock-on because the critical flow velocity decreases. All of these features are most likely related to the manner in which the unsteady shear layer develops along the cavity. Presumably, for deeper cavities, the occurrence of large-scale vortex formation proceeds in a relatively uninhibited fashion, whereas for the shallowest cavity, it may not occur. This aspect will be addressed in a forthcoming investigation.

#### 4.3.2. Short inlet pipe-cavity system

A short inlet pipe to the cavity system was employed to: (i) examine the consequence of a smaller characteristic thickness of the inlet boundary layer; (ii) address the consequence of a higher value of absolute frequency for the lowest pipe-cavity resonant modes, i.e.,  $N = 1-3$ ; and (iii) resolve the manner in which widely spaced resonant modes, which are attainable for the short-pipe system, influence the onset of flow tones, relative to the closely packed modes existing in the long-pipe-cavity system, shown in Figs. 4a–f.

The top image of Fig. 5a represents the case of the deepest cavity. Clearly defined peaks of pressure occur at resonant pipe modes centered approximately at 550, 1100, and 1600 Hz. These excited modes are clearly much more widely spaced than for the corresponding case of the long-pipe-cavity system shown in the top image of Fig. 4a. Two remarkable similarities exist, however, between the plots of Figs. 5a and 4a. First of all, the value of inflow velocity  $U$  for the onset of a clearly definable peak of pressure amplitude is of the order of 70 ft/s for both cases of Figs. 5a and 4a. This similarity is perhaps more evident by comparing the plan view of pressure amplitude on the plane of velocity versus frequency, represented by the bottom image of Fig. 5a, with the corresponding image at the bottom of Fig. 4a. Note that, at a given velocity, as many as three well-defined peaks exist; moreover, they are, in an approximate sense, harmonically related. This suggests that multiple Strouhal modes may coexist in the separated shear layer. In the absence of an acoustic resonator, it is known that an unstable shear layer can exhibit a number of coexisting, well-defined frequency components as shown by Knisely and Rockwell (1982).

The second notable feature of the plots of Fig. 5a is that the dominant resonant mode in Fig. 5a is of the order of 550 Hz, while in Fig. 4a, the excited modes extend from approximately 300–600 Hz. The same range of frequencies is therefore associated with the generation of large-amplitude pressure peaks. This observation, which suggests that the same mechanism of shear-layer instability is present in both cases, will be addressed subsequently. The plan view of

pressure amplitude  $p$  shown in the bottom image of Fig. 5a exhibits a black line passing through the peak pressure amplitude. As in the previous cases for the long-pipe-cavity system, this line corresponds to a constant value of  $fL/U$ .

In Fig. 5b, the top image shows further features of the pressure amplitude response, in the form of  $\log p$  on the plane of velocity  $U$  versus frequency  $f$ . In this plot, the increase in amplitude of the pressure fluctuation as flow velocity increases is clearly evident. Regarding this plot at the bottom of Fig. 5b, a number of sharp changes in sign of  $\partial(\log p)/\partial U$  occur along each band of constant frequencies as velocity is increased. As in the corresponding figures for the long-pipe-cavity system, the abrupt change in color corresponds to the locations of the peaks.

For the case of a shallower cavity, represented by  $W^* = 0.5$  and shown in Fig. 5c, the overall response characteristics are generally similar to those of the deeper cavity of Fig. 5a. Considering, first of all, the top image of Fig. 5c, the pressure peaks are not quite as consistent with variations of velocity, relative to those of Fig. 5a. With regard to the plan

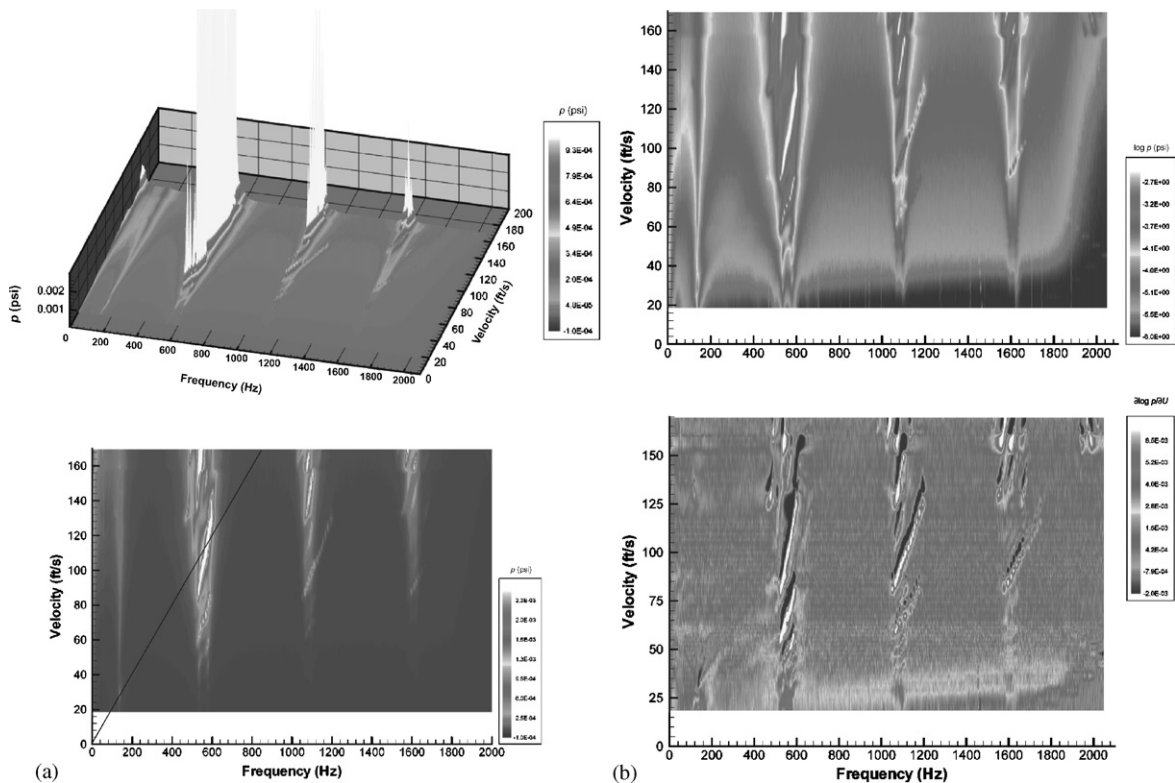


Fig. 5. (a) Isometric view (top image) and plan view (bottom image) of pressure amplitude as a function of frequency and velocity. Line shown on plan view represents a fit through peak values of pressure amplitude. Cavity length  $L^* = L/D = 2.5$  and depth  $W^* = W/D = 1.25$ , where  $D$  is pipe diameter. Short pipes of equal length are located at either end of the cavity. (b) Plan view of logarithmic pressure amplitude as a function of velocity and frequency (top image); and plan view of magnitude of the derivative of the logarithmic pressure amplitude with respect to velocity,  $\partial(\log p)/\partial U$  (bottom image). Cavity length  $L^* = L/D = 2.5$  and depth  $W^* = W/D = 1.25$ , where  $D$  is pipe diameter. (c) Isometric view (top image) and plan view (bottom image) of pressure amplitude as a function of frequency and velocity. Line shown on plan view represents a fit through peak values of pressure amplitude. Cavity length  $L^* = L/D = 2.5$  and depth  $W^* = W/D = 0.5$ , where  $D$  is pipe diameter. Short pipes of equal length are located at either end of the cavity. (d) Isometric view of logarithmic pressure amplitude as a function of velocity and frequency (top image); and plan view of magnitude of the derivative of the logarithmic pressure amplitude with respect to velocity,  $\partial(\log p)/\partial U$  (bottom image). Cavity length  $L^* = L/D = 2.5$  and depth  $W^* = W/D = 0.5$ , where  $D$  is pipe diameter. (e) Isometric view (top image) and plan view (bottom image) of pressure amplitude as a function of frequency and velocity. Line shown on plan view represents a fit through peak values of pressure amplitude. Cavity length  $L^* = L/D = 2.5$  and depth  $W^* = W/D = 0.25$ , where  $D$  is pipe diameter. (f) Plan view of logarithmic pressure amplitude as a function of velocity and frequency (top image); and plan view of magnitude of the derivative of the logarithmic pressure amplitude with respect to velocity,  $\partial(\log p)/\partial U$  (bottom image). Cavity length  $L^* = L/D = 2.5$  and depth  $W^* = W/D = 0.25$ , where  $D$  is pipe diameter. (g) Isometric view (top image) and plan view (bottom image) of pressure amplitude as a function of frequency and velocity. Line shown on plan view represents a fit through peak values of pressure amplitude. Cavity length  $L^* = L/D = 2.5$  and depth  $W^* = W/D = 0.125$ , where  $D$  is pipe diameter.

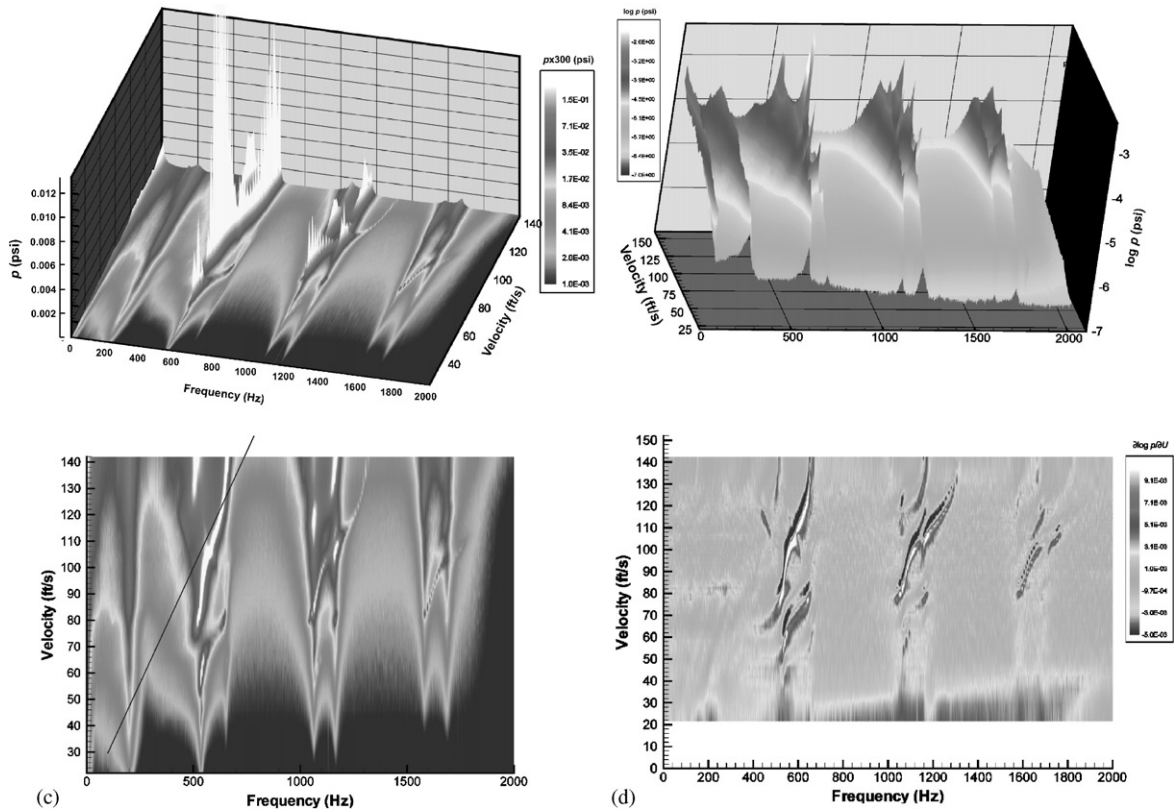


Fig. 5 (continued).

view of the pressure amplitude  $p$ , shown in Fig. 5c, the value of velocity for the onset of the first, large amplitude peak, is of the order of  $U = 100$  ft/s. This compares with an approximate value of  $U = 120$  ft/s for the first, large amplitude peak of Fig. 4c.

The plot of logarithmic pressure amplitude  $\log p$  shown in the top image of Fig. 5d clearly shows the increase in background amplitude with the increase of velocity and the emergence of well-defined peaks above the background level at sufficiently high values of velocity. The variation of the amplitude of  $\partial(\log p)/\partial U$ , shown in the bottom image of Fig. 5d, exhibits correspondence between abrupt changes in slope (i.e., gray level) and the pressure amplitude peaks evident in the plan view of the bottom image of Fig. 5c.

If the cavity depth  $W$  is decreased still further to a value of  $W^* = 0.25$ , as represented by the images of Fig. 5e, sharply defined pressure peaks are still evident. At the same value of  $W^* = 0.25$  for the long inlet pipe, shown in Fig. 4e, such sharply defined peaks do not occur. Note, however, that the peak occurring at the lowest value of velocity in the top image of Fig. 5e, further evident in the bottom image of Fig. 5e, is within the band of approximately 500–600 Hz. For the case of the long inlet pipe, shown in Figs. 4a and c, resonant peaks occur in this same band of frequencies. A similar instability mechanism therefore appears to be operative in both cases. The instability mechanism most likely associated with the generation of large-scale vortical structures will be addressed subsequently. The manner in which these large-scale structures develop may be a function of the momentum thickness  $\theta_0$  at separation, which, as described in Section 3, differs for the long and short inlet pipes. The momentum thickness  $\theta_0$  of the short-pipe system is one-third that of the long pipe–cavity system. A further factor that may influence the difference between Figs. 4e and 5e is the difference of damping of the long- and short-pipe–cavity systems.

The variation of the logarithmic pressure amplitude,  $\log p$ , over the velocity versus frequency plane, is represented by the top image of Fig. 5f. The increase in the pressure amplitude, along a line of constant frequency, say a frequency of the order of 500 Hz, is evident at a relatively low value of velocity  $U$  of the order of 35 ft/s; this situation contrasts with excitation of sharply defined peaks at higher velocities. This observation suggests that an inherent instability mode of the shear layer is effective in buffeting the resonator of the pipe–cavity system at lower values of velocity. Confirmation of the peaks of pressure amplitude, which are indicated in the bottom image of Fig. 5e, is evident in the abrupt change

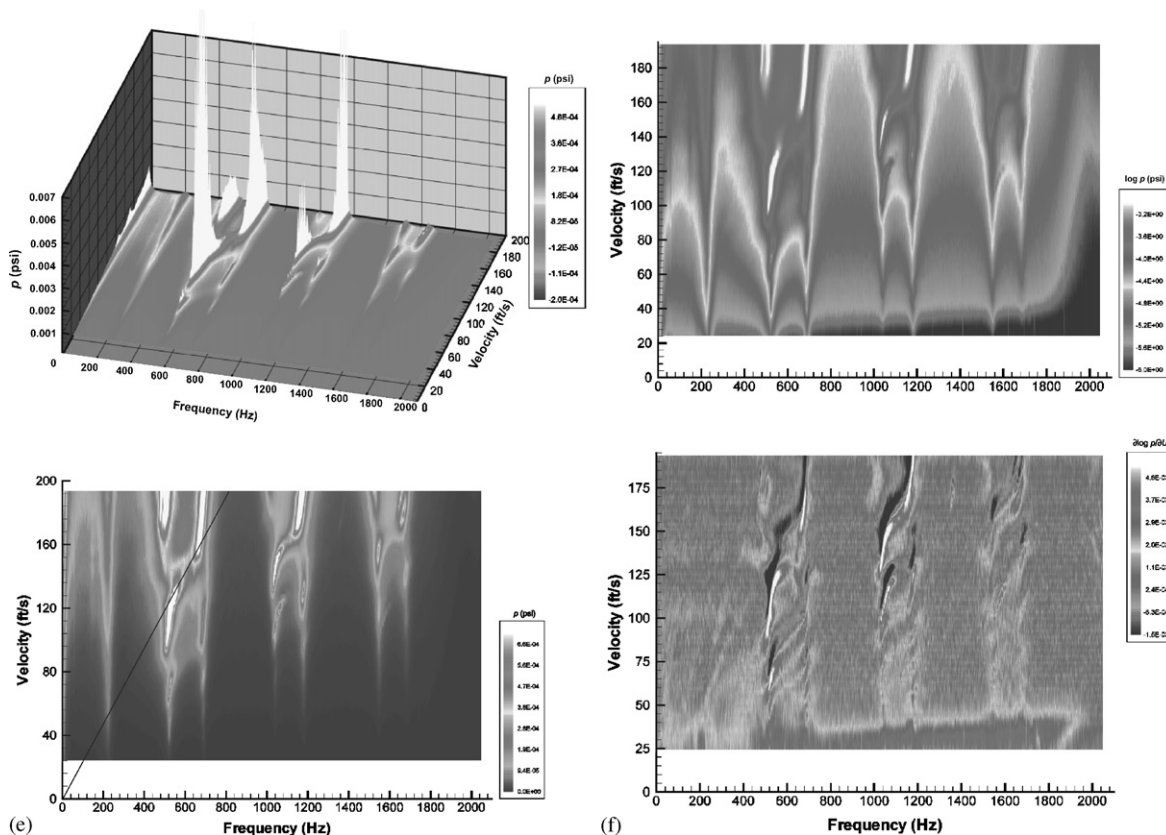


Fig. 5 (continued).

in sign of  $\partial(\log p)/\partial U$  in the bottom image of Fig. 5f. Moreover, this parameter  $\partial(\log p)/\partial U$  brings out additional peaks at lower value of flow velocity for the first two resonant modes; these peaks are not evident in the raw pressure plot at the bottom of Fig. 5e.

Finally, the case of the shallowest cavity,  $W^* = 0.125$ , is represented in Fig. 5g. The values of pressure amplitude generally remain very small, of the order of  $2 \times 10^{-4}$  psi. Moreover, sharply defined peaks are not evident. It is possible, however, to identify a broader peak, as shown in the plan view of the bottom image of Fig. 5g; this broader peak serves as the basis for the construction of a black line representing a constant value of  $fL/U$ . This peak, as well as others that might be inferred from the bottom image of Fig. 5g, are not sufficiently sharp to produce a consistent pattern of large gradients of  $\partial(\log p)/\partial U$ , evident from examination of the corresponding image of these gradients, which is not shown herein.

4.4. *Scaling of pressure fluctuations: amplitude limits and conditions for onset, persistence, and suppression*

In the foregoing sections, emphasis has been on the description of the organized peaks of pressure fluctuations that emerge above the background. These pronounced peaks are evident in most of the three-dimensional (isometric) plots of the respective images of Figs. 4a–g. In the summaries that follow, the focus is on the dimensionless representations that dictate the onset and existence of well-defined peaks. They are: dimensionless frequencies; dimensionless cavity length and depth; dimensionless pressure amplitudes; and values of velocity. All of these parameters are characterized using detectable peaks in Figs. 4a–g.

The modes of oscillation observed in the present investigation are defined as large-scale modes. That is, the present emphasis is on oscillations occurring for a limiting value of cavity length  $L_m$ , such that for a sufficiently deep cavity, the fully evolved axisymmetric instability mode is allowed to develop. As indicated in the foregoing, this asymptotic case corresponds to the largest pressure amplitudes observed in preliminary experiments over a range of cavity length. In

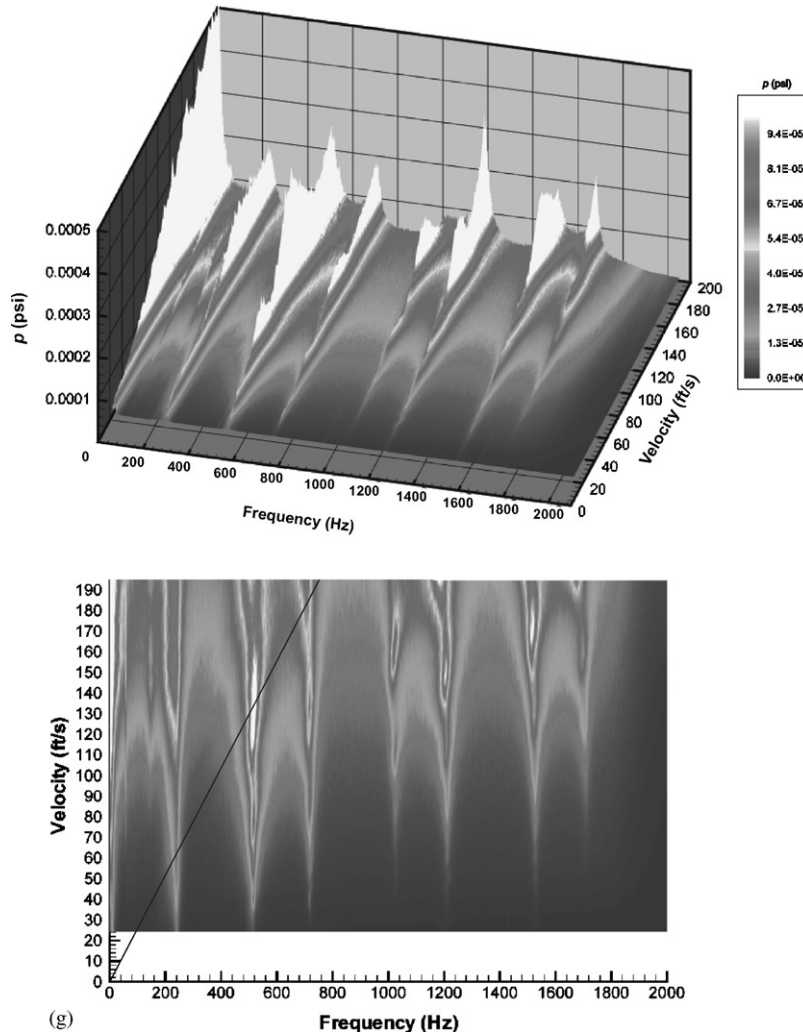


Fig. 5 (continued).

view of the fact that they occur for relatively long cavities, i.e., cavities of length  $L$  significantly larger than the pipe (or jet) diameter  $D$ , these oscillations are designated as large-scale modes. Furthermore, as will be addressed, when the frequencies at which the peaks occur are scaled according to  $fD/U$ , then the values lie within a range corresponding to fully evolved (large-scale) vortex formation in an unbounded free-jet. This observation provides a further reason for characterizing these oscillations as large-scale modes along sufficiently deep cavities. In the following, several characteristics of these large-scale modes are addressed.

#### 4.4.1. Frequency of oscillation

Considering the data shown in Figs. 4a–g, the values of frequency for the observed peaks extend over the range of approximately 300–600 Hz. In turn, these frequencies correspond approximately to dimensionless values in the band  $0.3 \leq fD/U \leq 0.6$ . This issue of frequency scaling is addressed in further detail at the end of Section 5, i.e., Section 5.2.

#### 4.4.2. Pressure amplitudes

The magnitude  $p$  of the pressure fluctuations is normalized by the dynamic pressure of the inflow, defined as  $\rho U^2/2$ , in which  $\rho$  is the density of air under standard conditions and  $U$  is the averaged centerline velocity, i.e.,  $U \equiv \bar{u}_m$ . This normalization involved the range of data for which detectable peaks were observed in Figs. 4a–g. Peak pressure amplitudes as high as  $p/(\rho U^2/2) \cong 0.6$  can be attained for the short inlet pipe, the deepest cavity, and a high inflow

velocity (Fig. 5a). At the other extreme, values as low as  $p/(\rho U^2/2) \cong 0.007$  were observed for the long inlet pipe, a moderate depth cavity, and a relatively low inflow velocity corresponding to the onset of an initial peak amplitude (Fig. 4c).

#### 4.4.3. Persistence of pressure peaks

Examination of the plots of Figs. 4a–g reveals that as the cavity depth  $W$  decreases, the peak pressure amplitude tends to decrease as well. Pronounced peaks can occur, however, at values of cavity depth as low as  $W/D = 0.25$ , i.e., even for very shallow cavities having a length to depth ratio of 10.

#### 4.4.4. Suppression of amplitude peaks

For values of cavity depth sufficiently small, pronounced amplitude peaks are no longer evident. This range of suppression occurs for  $W^* = W/D \gtrsim 0.125$ . It should be noted, however, that the occurrence of preferentially excited pipe modes is still identifiable at  $W^* = 0.125$ , over the aforementioned range of frequencies falling roughly in the band  $0.3 \lesssim fD/U \lesssim 0.6$ . These preferentially excited modes exist in absence of any apparent lock-on.

#### 4.4.5. threshold velocities

Considering the range of data exhibited in Figs. 4a–g, the velocities for onset of pronounced peaks, accounting for both short and long inlet pipes, range from approximately 70–120 ft/s. These velocities represent the values required to trigger the first amplitude peak, and presumably the first occurrence of a flow tone (addressed in Section 6), over a range of cavity depths, for both short and long inlet pipes. Dimensionless representations of these velocities, based on power concepts, is currently under consideration. In essence, one expects the vorticity-based contribution to the acoustic power  $P_{ac}$  to scale according to  $P_{ac} \sim \rho U^2 u_{ac}$  for a given value of cavity length  $L$ . Sufficiently large values of  $P_{ac}$  can be achieved either by increasing the value of inflow velocity  $U$  or the self-excited acoustic velocity  $u_{ac}$ . These features must be taken into consideration for dimensionless representation.

#### 4.4.6. Preferred modes of resonator

The foregoing considerations have addressed the scaling and limiting values of the system parameters. An additional consideration is the determination of whether all modes of the acoustic resonator, i.e., pipe–cavity system, are susceptible to coupling phenomena that lead to generation of flow tones. For the entire range of experiments, tones are generated only for the even modes  $N$  of the pipe–cavity system. This observation is compatible with the existence of a pressure node and a velocity antinode at the location of the cavity. An interpretation of the excitation of even modes is as follows. Effective perturbation of the separating shear layer requires relatively large amplitudes of acoustic velocity fluctuations in the vicinity of shear layer separation, i.e., in the most sensitive, or receptive, region of the shear layer along the mouth of the cavity. This occurs for even resonant modes. With this concept in mind, an interesting issue is the effect of asymmetry of the pipe sections located at either end of the cavity, and whether a small amount of asymmetry can effectively attenuate the amplitude of the self-excited oscillations, presumably by displacing the pressure node, i.e., the velocity antinode, away from its most effective location. This matter will be addressed in a forthcoming investigation.

## 5. Frequencies of oscillation: correlation and scaling

Identifiable peaks in the data given in Section 4.3, and the manner in which they vary with either inflow velocity or cavity length, provide a basis for: (i) correlations with traditional models; and (ii) frequency scaling based on concepts of inviscid stability. In the following, these two classes of assessments are addressed in detail.

### 5.1. Correlations of frequencies of oscillation with existing models based on cavity length

#### 5.1.1. Overview of models

Over the years, a great deal of effort has been devoted to the development and revision of models for the dimensionless frequency of oscillation. They have the general form

$$fL/U = (U_c/U)(n \pm a_0), \quad (5.1)$$

in which  $U$  is taken to be the freestream velocity,  $U_c$  is the convective speed of a vortex or instability wave through the shear layer,  $n$  is the stage of oscillation and  $a_0$  is a constant. This type of model has its genesis in the early formulations of Rossiter (1962, 1964), whose more general formulation accounted for variations of Mach number, and Powell (1961,

1964), who actually employed this type of relationship for a jet–edge, as opposed to a cavity configuration. In the application of most models, the ratio  $U_c/U$  and  $a_0$  are viewed to be adjustable constants. Various types of arguments have been made, however, for relating the dimensionless phase velocity  $U_c/U$  to values determined from stability theory. In doing so, however, a constant value of  $U_c/U$  is defined; in contrast, inviscid spatial stability theory indicates that  $U_c/U$  is actually a function of frequency. Recent efforts in the theoretical direction aim to specify values of  $U_c/U$  and  $a_0$  without recourse to empiricism. Such models employ an infinitesimally thin shear layer. They include the work of Crighton (1992) for the case of a jet–edge configuration and Howe (1997, 1998) for edge and cavity configurations.

For purposes of correlating the present experimental data, the following relations will be employed: (a)  $fL/U = 0.61(n - \frac{1}{4})$ , which is due to Elder (1978) and Pollack (1980); (b)  $fL/U = 0.6(n - \frac{1}{6})$ , which is due to Howe (1997, 1998); and (c)  $fL/U = 0.6n$ , which serves as a reference correlation that does not account for any end effects, i.e.,  $a_0 = 0$ . This correlation was also deduced on the basis of phase measurements by Rockwell and Schachenmann (1982).

It should be emphasized that the correlations (a) and (b) have been employed almost exclusively for the case where there is a well-defined freestream, as opposed to the present situation of flow through a pipe. When the pipe flow is fully developed, a freestream velocity does not exist. The characteristic velocity,  $0.86U = 0.86\bar{u}_m$ , which represents the spatially averaged or bulk-averaged velocity through the pipe, is employed herein. It should be noted that use of this normalizing velocity  $0.86U$  could also be interpreted as follows. It is equivalent to employing an equivalent freestream velocity  $U$  and a lower value of the dimensionless phase speed  $0.86U_c/U$ .

### 5.1.2. Correlations for variations of inflow velocity

Figs. 6a–c show comparisons between the correlations of Section 5.1.1 and the data of Figs. 4a–e, which exhibit well-defined peaks. In each figure, the top plot represents a best fit through the data of the form  $fL/U = K$ , in which  $K$  is simply the constant that provides the best linear fit. In other words, this fit does not involve any of the aforementioned correlations. In the bottom plot of each figure, direct correlation with the foregoing models (a)–(c) is given. In all figures presented herein, the normalizing velocity is  $0.86U = 0.86\bar{u}_m$  which, as described in the previous section, corresponds to the bulk velocity at the pipe exit.

Fig. 6a represents the case of the deepest cavity  $W^* = 1.25$ . The top plot shows that the normalized frequencies  $fL/U$  are related to each other in an approximately harmonic fashion. The lower plot of Fig. 6a shows correlations with stages  $n = 2, 4$ , and  $6$ . Reasonable agreement is attained with the correlation  $fL/(0.86U) = 0.6n$ .

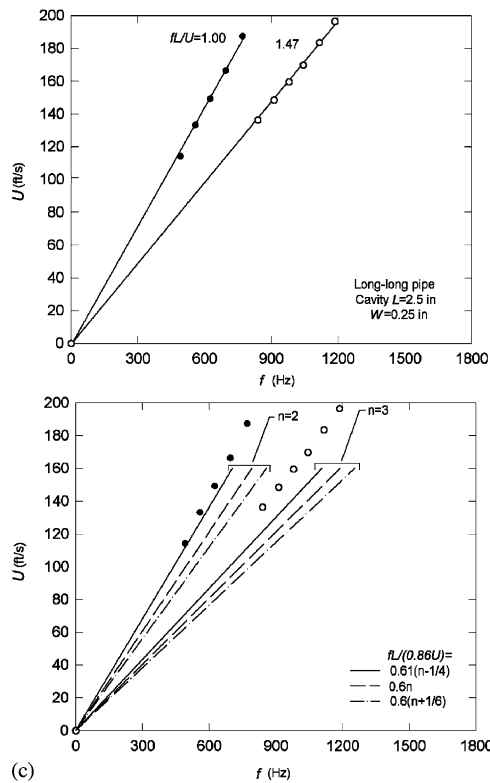
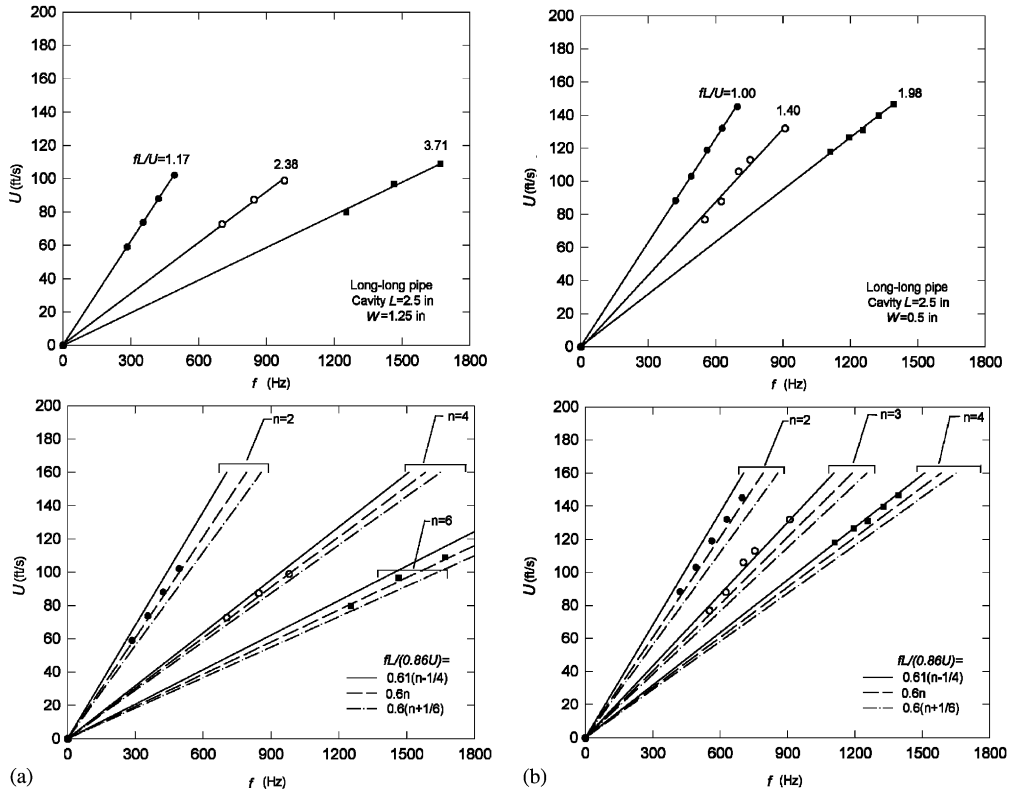
The correlations of Fig. 6b correspond to the shallower cavity  $W^* = 0.5$ . In this case the upper plot shows fits according to  $fL/U = 1.00, 1.45$  and  $1.98$ . In other words, in addition to a harmonic mode, an apparent intermediate mode  $fL/U = 1.45$  exists. In the lower plot of Fig. 6b, however, the data are reasonably well fitted using stage, or mode, numbers  $n = 2, 3$  and  $4$  and with the value of the constant  $a_0 = \frac{1}{4}$ .

For the case of the shallowest cavity,  $W^* = 0.25$ , for which detectable peaks could still be identified, the data are represented in Fig. 6c. The correlation at the top of Fig. 6c shows that harmonics of the fundamental mode  $fL/U = 1.0$  are not present. Rather, only a so-called intermediate mode  $fL/U = 1.47$  is apparent. As indicated in the bottom plot of Fig. 6c, the case of  $n = 2$  is correlated for the equation with ( $a_0 = \frac{1}{4}$ ), while neither  $n = 2$  or  $n = 3$  shows an acceptable correlation with the intermediate mode, represented as  $fL/U = 1.47$  in the corresponding upper plot of Fig. 6c.

### 5.1.3. Coexistence of multiple modes

A common feature of the correlations discussed in Sections 5.1.2 is the coexistence of two or more frequency components at a given value of velocity  $U$ . The criterion employed for defining these frequency components simply involves detection of an organized peak(s) in the pressure spectrum. These peaks are associated with the hydrodynamic unsteadiness of the shear layer past the cavity. In other words, only selected frequency components in the corresponding figures of Section 5.1.2 represent flow tones for which the organized unsteadiness of the shear layer, i.e., a Strouhal mode, couples with the acoustic resonant mode of the pipe–cavity system.

It is important to recognize that multiple hydrodynamic modes can exist in absence of acoustic resonant phenomena. This is evident from the early correlations of Rossiter (1962, 1964) for the limiting case of zero Mach number, and the wide range of theoretical and experimental investigations of impinging flows over the past two decades, including not only cavity, but also jet–edge and jet–orifice systems. Most recently, the theoretical model of Howe (1997) analyzes, using a vortex sheet representation, the multiple modes present for the case of flow past a cavity at low Mach number. As shown by Knisely and Rockwell (1982), actual experimental characterization of the unstable shear layer past a cavity, emerging from initially laminar conditions, shows the existence of a substantial number of frequency components at a given value of cavity length. These multiple frequency components need not be harmonically related to each other; in fact, sum and difference frequency components are also present. Such strictly hydrodynamic considerations provide a basis for interpreting the multiple frequency components, or modes, present at a given value of



inflow velocity  $U$  in Section 5.1.2. Detectable frequency components generally line up with one of the resonant acoustic modes of the pipe–cavity system. If conditions are appropriate for coupling, a pronounced flow tone may result.

### 5.2. Scaling of frequency of oscillation on basis of jet diameter

The correlations of the preceding section attempt to provide overall guidance for the occurrence of self-sustaining oscillations in accordance with variations of inflow velocity. An alternate, and more rigorous, indicator of the origin of the oscillation involves scaling the frequencies on the basis of stability concepts. It should be emphasized again that, for all cases considered herein, the inflow is fully turbulent, and it is assumed that application of inviscid stability theory to the time-averaged base flow, which itself is influenced by the presence of turbulence, can provide guidance for determining the frequency of the predominant fluctuation. This type of scaling is based on a representative thickness of the shear layer, in contrast to the use of a geometrical scale such as cavity length or depth. These scaling parameters are: momentum thickness  $\theta_0$ , evaluated at the exit of the inlet pipe (see Section 3); and the pipe diameter  $D$ , which is an approximation to the jet diameter, i.e., the distance between the inflection points of the jet shear layer. Generally speaking, use of the momentum thickness  $\theta_0$  is most relevant for the case of a thin shear layer instability, which initially occurs in the immediate vicinity of the nozzle exit, and is expected to give rise to formation of smaller-scale vortices. On the other hand, the jet diameter  $D$  provides a suitable scale for a fully evolved instability of the entire jet, typically associated with large-scale vortex formation.

The present emphasis is on the large-scale mode of oscillation. This mode is defined to occur at a long cavity length, which allows development of a fully evolved axisymmetric instability (Section 4.4). It is expected to scale on the jet diameter  $D$ . Considerable experimental work for the case of a free axisymmetric jet subjected to loudspeaker excitation or, alternately, to feedback from an impinging jet, allows one to deduce the predominant frequency  $fD/U$ , which is taken to represent the generation of large-scale vortical structures, often referred to as “puffs”. These experiments, along with an overall correlation of the data, are described by Blake (1986). Relevant investigations include Browand and Laufer (1975), Crow and Champagne (1971), Lau et al. (1972), and Nossier and Ho (1982), each of which has a different degree of development and thickness of the boundary layer at the nozzle exit. Based on this range of experimental studies, the dimensionless frequency of the large-scale vortex formation in the jet is expected to lie in the range of  $0.3 \leq fD/U \leq 0.6$ .

Scaling of the frequencies of the predominant peaks exhibited in Figs. 4a–g according to  $fD/U$  showed that they generally lie in the range of  $0.35 \leq fD/U \leq 0.4$ . These values are in remarkable agreement with the expected values of  $0.3 \leq fD/U \leq 0.6$  defined in the foregoing. Fig. 7 exhibits the data corresponding to the predominant amplitudes, which have dimensionless frequencies  $fD/U$  in this range. This plot emphasizes the collapse of the data for different thicknesses of the inflow boundary layer, and its relative invariance with flow velocity, or more appropriately, with Reynolds number  $UD/\nu$ .

Perhaps the most remarkable observation, if one views the entire set of data, is that the scaling relation  $fD/U$  proves accurate irrespective of the cavity depth. That is, the unstable frequency of these so-called large-scale modes is  $fD/U \cong 0.4$ , even for relatively shallow cavities for which large-scale vortex formation is not expected to occur. Peaks of the large-scale mode at  $fD/U \cong 0.4$  are detectable for values of cavity depth as small as  $W/D = 0.25$ . Moreover, even for the shallowest cavity  $W/D = 0.125$ , for which pronounced peaks do not occur, the excitation of the pipe modes shows preferential values clustered in the vicinity of  $fD/U = 0.4$ . Details of the development of this instability, and mechanisms for sustaining it, deserve further consideration.

In this regard, the possible existence of a global (absolute) instability should be addressed. It contrasts with the aforementioned instabilities, which are of the convective type. In essence, this type of instability is likely to occur in

Fig. 6. (a) Plots of values of frequency corresponding to amplitude peaks in Figs. 4a and b. Top plot shows lines corresponding to the best fit of the dimensionless frequency  $fL/U$  through each set of data points. Bottom plot shows lines corresponding to three different correlations for  $fL/U$ . Velocity  $U$  corresponds to the time–mean centerline velocity at the center of the pipe, i.e.,  $U = \bar{u}_m$ . In the lower plot, the bulk velocity of the pipe flow,  $0.86U$ , is employed as the normalization velocity. (b) Plots of values of frequency corresponding to amplitude peaks in Figs. 4c and d. Top plot shows lines corresponding to the best fit of the dimensionless frequency  $fL/U$  through each set of data-points. Bottom plot shows lines corresponding to three different correlations for  $fL/U$ . Velocity  $U$  corresponds to the time–mean centerline velocity at the center of the pipe, i.e.,  $U = \bar{u}_m$ . In the lower plot, the bulk velocity of the pipe flow,  $0.86U$ , is employed as the normalization velocity. (c) Plots of values of frequency corresponding to amplitude peaks in Fig. 4e. Top plot shows lines corresponding to the best fit of the dimensionless frequency  $fL/U$  through each set of data-points. Bottom plot shows lines corresponding to three different correlations for  $fL/U$ . Velocity  $U$  corresponds to the time–mean centerline velocity at the center of the pipe, i.e.,  $U = \bar{u}_m$ . In the lower plot, the bulk velocity of the pipe flow,  $0.86U$ , is employed as the normalization velocity.

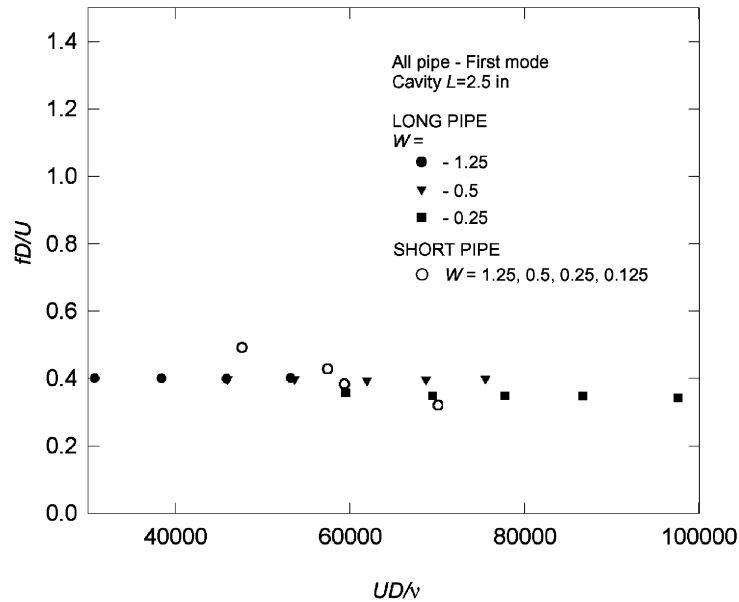


Fig. 7. Superposition of values of dimensionless frequency corresponding to the maximum amplitude peaks for each cavity configuration.

configurations where regions of negative streamwise velocity occur as a result of, for example, the local reverse flow in the recirculation zone in a shallow cavity. In an analogy with the corresponding global (absolute) instability occurring in the wake behind a cylinder of diameter  $D$ , for which the instability scales according to  $fD/U$ , it is expected that the cavity unsteadiness would scale according to  $fW/U$  if it is globally unstable. That is, the only representative transverse length scale would be the cavity depth  $W$ . Preliminary indications suggest that such a global instability does not exist, since the frequency scales remarkably well according to  $fD/U = 0.4$  for all values of cavity depth  $W$ . Scaling of the form  $fW/U$  would produce a five-fold variation of the values of  $fW/U$ , corresponding to the range of  $W/D$  extending from 1.25 to 0.25. Nevertheless, the role of the recirculation zone in maintaining the cavity oscillations is worthy of further consideration.

## 6. Onset of locked-on flow tones

A primary issue is whether highly coherent, locked-on flow tones can arise in the presence of a fully turbulent inflow, as described in the references cited in Section 1. Nearly, all previous investigations of this class of flows have considered the case of laminar, transitional, or undefined inflow conditions. Moreover, even in those limited cases where the inflow boundary layer was fully turbulent, means to characterize the onset of lock-on were not explicitly addressed using a simple criterion.

### 6.1. General features of lock-on

It is generally accepted that locked-on flow tones exhibit the following characteristics:

(a) *Amplitude increase with increase of inflow velocity.* An abrupt increase in amplitude of the unsteady pressure occurs as the flow velocity is increased in the region of the onset of lock-on. It is expected that, if spatial resolution along the velocity coordinate is adequate, the plot of unsteady pressure amplitude versus velocity will not necessarily be a discontinuity. Rather, it should be possible to characterize a slope of peak pressure amplitude  $P$  versus  $U$  associated with the occurrence of locked-on flow tones. This slope could be considered as a deviation from the slope prior to the onset of lock-on, where it is due to a change in either the background turbulence level or an underlying coherent instability, i.e., the Strouhal source.

(b) *Amplitude peak above background.* Attainment of sufficiently high amplitude of the pressure peak  $P$  above the background pressure level  $p_{bg}$  would be a further criterion for identification of a locked-on flow tone. As noted in (a), this background pressure amplitude would be due to either the underlying turbulence or the inherent instability (Strouhal source), or a combination of them. It is expected that the incompressible pressure amplitude due both to turbulence and to the inherent instability will change with velocity according to a power law. The exponent in the power law would take on different values for each of these two origins. It is, however, difficult to decompose the background pressure into turbulence and inherent instability components, due to the manner in which the instability wave grows upon the turbulent background. Nevertheless, it would be desirable to characterize the peak pressure amplitude  $P$  that occurs for locked-on flow tones in terms of a value of excess pressure above the background  $p_{bg}$ , i.e., turbulence/inherent instability wave components. An important issue regarding the pressure amplitude is the fact that not only the magnitude of the inherent instability (Strouhal source), but also the magnitude of the turbulence will be enhanced by the presence of a resonator, even when lock-on does not occur. It is therefore desirable to have a criterion that would allow a straightforward estimate of the maximum attainable pressure amplitude due to turbulent/instability excitation of a resonator in the absence of lock-on; then, any excess pressure  $p$  above this value would presumably be associated with the lock-on features of the inherent instability (Strouhal source).

(c) *Frequency coincidence.* Coincidence of the frequency of the inherent instability wave, which presumably gives rise to vortex formation, with the frequency of a given mode of the resonator, is a further criterion for the occurrence of locked-on flow tones. In situations where the inflow is laminar, it is relatively easy to distinguish between the frequency of the inherent instability and the resonator frequency prior to the occurrence of lock-on. Although well-defined peaks due to both of these origins may exist in the region away from lock-on, a single frequency occurs during lock-on. In the event that the inflow is fully turbulent, the frequency of the inherent instability is more difficult to detect. In fact, a pre-existing coherent oscillation may not be readily detectable prior to coupling with the resonator.

## 6.2. Nonlocked-on buffeting of a resonator: a mechanical analogy

Incompressible turbulence or an instability wave can effectively excite a resonator. A consequence of this excitation may be a detectable peak or bump in the spectrum of the pressure fluctuation. A mechanical analogy to this process involves flow–structure interaction, or more explicitly, turbulent buffeting of an elastically mounted body. Whereas very little effort has been devoted to understanding the nature of turbulent buffeting of a resonator, the buffeting of a body or structure has received considerable attention. It can serve as a basis for characterizing the limiting pressure amplitude due to turbulent buffeting of a resonator.

Consider a discrete mechanical system with a mass  $m$ , a spring having a stiffness  $C$ , and a dashpot having damping coefficient  $B$ . This system has a natural frequency  $f_n \equiv \omega_n/2\pi$ . The  $Q$ -factor of this mechanical system is determined by the damping coefficient  $\zeta$ , i.e.,  $Q = \frac{1}{2}\zeta$ . This system may be excited by, for example: a relatively broadband turbulence, a combination of turbulence and an instability wave; or simply an instability in the form of a vortex. Irrespective of the type of excitation, one may represent the spectrum of the consequent turbulent/instability force  $F$  as  $S_F(f)$ . The mechanical admittance  $\chi_m$  of the system is, in accordance with the terminology of Naudascher and Rockwell (1994):

$$|\chi_m(\omega)| = [1/C] / \{ [1 - (\omega/\omega_n)^2]^2 + [\omega/Q\omega_n]^2 \}^{1/2} \quad (6.1)$$

in which  $C$  is the mechanical stiffness of the spring. The relationship between the spectrum of the displacement response  $S_x(f)$  and the turbulent forcing function is simply:

$$S_x(f) = |\chi_m(f)|^2 S_F(f). \quad (6.2)$$

The form of  $S_F(f)$  is arbitrary. According to Eq. (6.1), for defined values of  $C$  and  $\omega_n$ , the magnitude of the displacement at a given value of frequency  $\omega = 2\pi f$  will be maximized when the value of  $Q$  takes on its largest value. In other words, when the  $Q$ -factor becomes large, it represents a very lightly damped system and the displacement amplitude becomes large. The converse holds, of course, when  $Q$  is small. An analogous relationship to Eq. (6.1), and similar reasoning, holds for a distributed (multi-degree freedom) resonator as well.

In a general sense, a fluid resonator can be considered analogous to the resonant structural system described in the foregoing. All resonators of the standing wave type are inherently distributed, rather than discrete. Nevertheless, these distributed resonators do have, at a single value of excitation frequency, a specific value of damping, or  $Q$ -factor. If an analogous linear relationship between spectra of the response pressure amplitude, resonator admittance, and the incompressible turbulence/instability wave exists in parallel with Eq. (6.2), it is possible to make the following, simple argument. Consider the schematic of the pressure spectrum and its  $Q$ -factor defined in Fig. 8. The response pressure amplitude at frequency  $f_0$ , i.e.,  $S_p(f_0)$ , due to buffeting of a resonator having a quality factor  $Q$  can itself have a maximum quality factor of  $Q$ . In other words, for the case of linearized, turbulent buffeting of a resonator, no

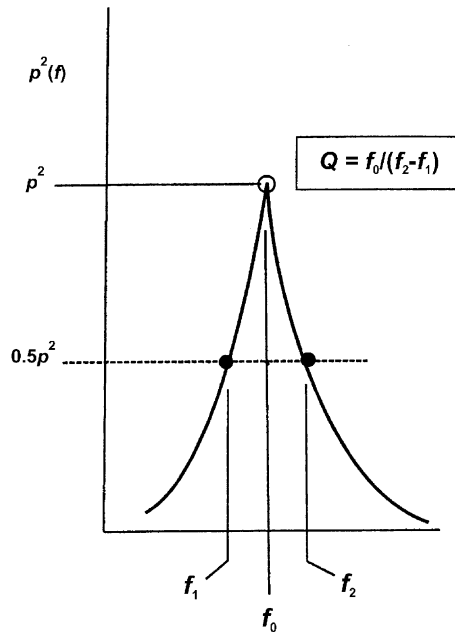


Fig. 8. Schematic illustrating definition of quality ( $Q$ ) factor based on pressure spectrum  $p^2(f)$ .

mechanism exists for inducing a pressure amplitude response having a  $Q$ -factor in excess of the  $Q$ -factor of the resonator, which is defined in Section 2.3. The maximum  $Q$ -factor of a resonator occurs in absence of mean flow, and these values are given in Section 2.3. The no flow value of  $Q$  would provide an upper (bounding) limit for the  $Q$ -factor of the pressure amplitude response, i.e., the  $Q$ -factor of the spectrum of the pressure. In essence, this means that if the spectrum of the response pressure has a  $Q$ -factor in excess of this upper bound, a mechanism for coupling, i.e., the onset of locked-on flow tone generation, must be present.

### 6.3. Criteria for evaluation of flow tone lock-on

The background information outlined in the foregoing leads to several criteria for characterizing the onset of locked-on flow tones. Generic cases were selected from the relatively large number of experiments described in Section 4.3. The following types of assessments are expected to lead to identification of locked-on flow tones: (a) variation, i.e., slope, of peak pressure amplitude  $P$  of the pressure spectrum as a function of inflow velocity  $U$ ; (b) value of the peak pressure amplitude  $P$  relative to the local amplitude of the background pressure  $p_{bg}$ ; (c) variation of the Quality ( $Q$ )-factor of the pressure spectrum as a function of either inflow velocity  $U$  or cavity length  $L$ ; this type of  $Q$ -factor is defined in Fig. 8. Emphasis herein will be on criteria (b) and (c).

### 6.4. Characterization of the onset of lock-on for a given resonant acoustic mode

The range of data described in Section 4.3 can be examined in order to determine the onset of lock-on, in accord with the approaches defined in Section 6.3. Of particular interest with regard to the onset and eventual attainment of lock-on are the following: (a) the consequence of cavity depth on the lock-on process and the nature of lock-on at a sufficiently large flow velocity, such that a relatively large pressure peak is generated; and (b) the initial onset of a locked-on state as flow velocity is varied. This initial state will most likely exhibit a relatively low amplitude peak of pressure amplitude. In the following, these features are addressed using selected data from Section 4.

#### 6.4.1. Effect of cavity depth on the lock-on of large-scale mode

Fig. 9a shows the variation of peak pressure amplitude  $P$  (determined from spectra  $p^2(f)$ ) and quality factor  $Q$  as a function of the flow velocity for various values of cavity depth  $W$ . The cavity length  $L^*$  has its largest value  $L_m^* = L_m/D = 2.5$  and is maintained constant. The plots of  $P$  in the left column are to be compared, respectively, with

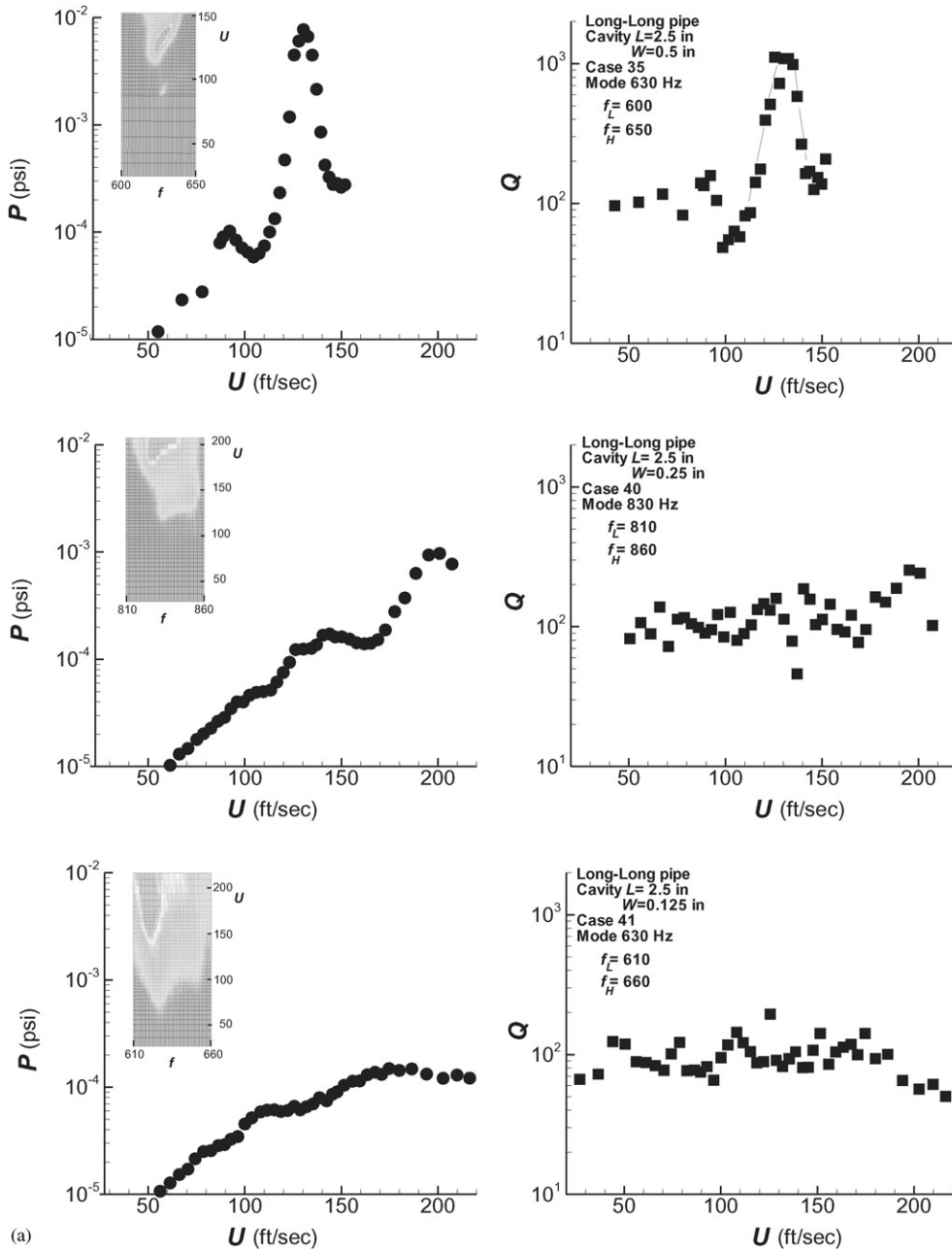


Fig. 9. (a). Effect of cavity depth on onset of flow tones. Plots show peak pressure amplitude  $P$  and quality factor  $Q$  as a function of centerline velocity  $U$  for data corresponding to Figs. 4c and d (top set of plots), 4e (middle set of plots), and 4f (bottom set of plots). Images in the inset of each pressure amplitude plot correspond to a zoomed-in version of a portion of the plan view of the aforementioned sets of plots. (b) Direct comparison of variations of peak pressure amplitude  $P$  with centerline velocity  $U$  corresponding to data of Fig. 9a.

Figs. 4c, e and f representing plots of cavity depths  $W^* = 0.5, 0.25,$  and  $0.125$ . The peak pressure amplitude  $P$  may occur at a frequency that deviates from the frequency of the resonant acoustic mode when flow velocity is increased. It is therefore necessary to search for the peak  $P$  over a defined band of frequencies at a given velocity. The lower and upper frequencies of this band are designated by  $f_L$  and  $f_H$ , and are defined in the inset of each figure. Moreover, a zoomed-in view, which corresponds to stretching of a portion of the image of amplitude response in a corresponding

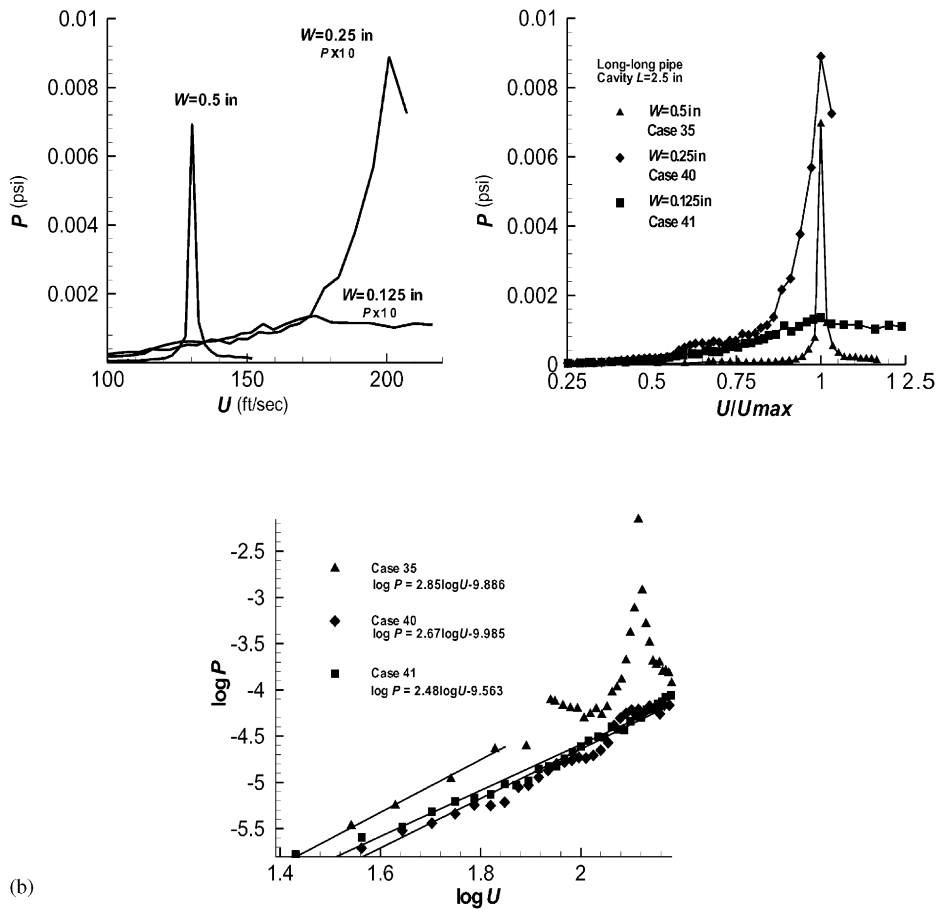


Fig. 9 (continued).

figure in Section 4, is provided for each of the plots in the left column of Fig. 9a. In each of these insets, the direction of increasing velocity is vertically upwards and the left and right margins correspond to values of  $f_L$  and  $f_H$ . Considering the peak magnitude in each of the pressure plots in the first column, it is evident that as the cavity depth is decreased, this amplitude decreases as well. Moreover, only for the deepest cavity,  $W^* = 0.5$ , represented by the top plot, does a well-defined peak region exist. Milder peaks are evident in the middle and bottom plots.

Variations of the  $Q$ -factor with velocity are given in the right column of Fig. 9a. The  $Q$ -factor is calculated from the spectrum,  $p^2(f)$  versus  $f$ , as defined in Fig. 8. Let  $f_0$  be the frequency at which the peak occurs and  $f_2$  and  $f_1$  represent the frequencies at which half-values of  $p^2(f)$  occur. The quality  $Q$ -factor is  $f_0/(f_2 - f_1)$ . As determined in the preliminary stage of this program, substantial uncertainties in  $Q$ -factor are unavoidable, as described in Section 2.3. The  $Q$ -factor plots of Fig. 9a therefore show significant deviations. For the top plot of the  $Q$ -factor, corresponding to the cavity depth  $W^* = W/D = 0.5$ , large values of  $Q$  of the order of  $10^3$  are attainable. Since the theoretically determined  $Q$ -factor for a simple pipe, in absence of both a cavity and throughflow, has a much lower value of approximately 80. In accordance with the discussion of Section 6.2, the peak having  $Q = 10^3$  is therefore taken to represent a locked-on flow tone. In contrast, at smaller values of cavity depths  $W^* = W/D = 0.25$  and  $0.125$ , discernible, small-amplitude and rounded peaks of the  $Q$ -factor are generally evident at locations of the corresponding mild peaks of the pressure amplitude distributions in the left column of Fig. 9a. It is clear, however, that sufficiently large  $Q$ -factor above the background value are not attained, and it is therefore concluded that no locked-on flow tone exists for these states. It should be cautioned, however, that these observations are only for the longest cavity length, for which the large-scale mode of vortex formation presumably becomes well developed. At short values of cavity length, where smaller-scale vortices may be present, locked-on states may be attainable. This issue is currently under investigation.

Fig. 9b provides further representations of the variation of peak pressure amplitude  $P$ . The top left plot directly compares  $P$  versus velocity  $U$ . Note that the values of  $P$  for the shallower cavities  $W^* = W/D = 0.25$  and  $0.125$  have been multiplied by a factor of 10 for this comparison. The case of the deepest cavity  $W^* = 0.5$  produces a sharply defined peak at a relatively low value of velocity  $U = 130$  ft/s. For the case of the shallower cavity  $W^* = 0.25$ , a peak is not obtained until a much higher velocity of  $U = 200$  ft/s and, moreover, this peak is not sharply defined. Finally, for the shallowest cavity  $W^* = 0.125$ , the peak is extremely mild at a velocity of approximately  $U = 170$  ft/s.

The upper right plot of Fig. 9b compares the shape of each peak on ordinates of peak amplitude  $P$  versus normalized velocity  $U/U_{\max}$ . This plot again brings forth the sharpest response for the deepest cavity. In the lower plot Fig. 9b, the plot of  $\log P$  versus  $\log U$  emphasizes the increase in the pressure amplitude prior to attainment of the pressure peak. Curves of approximately the same slope are fitted through each set of data for each value of cavity depth  $W$ .

#### 6.4.2. Initial states of lock-on

The series of plots shown in Fig. 10 address the nature of the initial locked-on state as the velocity is varied for several representative inflow and cavity configurations. Often, these states have relatively low amplitude peaks. The pressure amplitude plots shown in the left column correspond, respectively, from top to bottom, to Figs. 4c, 5c, and 4a. The top and bottom plots of peak pressure amplitude  $P$  versus flow velocity  $U$  in Fig. 10 compare the effect of cavity depths  $W^* = W/D = 0.5$  and  $1.25$ . It is evident that, for the larger value of cavity depth  $W^* = 1.25$ , the onset of a first, pronounced pressure peak occurs at a relatively low inflow velocity of the order of  $U = 70$  ft/s (bottom plot), in comparison with the case  $W^* = 0.5$ , for which the first peak is at  $U = 120$  ft/s (top plot). The presumption is that the deeper cavity allows more effective development of a large-scale vortex over the relatively long cavity. This feature, along with the larger degree of distortion of the trajectory of the acoustic particle velocity near the leading- and trailing-corners of the deeper cavity, may yield more effective generation of acoustic power (Howe, 1975, 1980; Stoneman et al., 1988). For both the  $W^* = 1.25$  and  $0.5$  cavities, the magnitude of the  $Q$ -factor shows a relatively large value at the location of the first peak.

The middle set of plots of Fig. 10 corresponds to the case of the cavity depth  $W^* = 0.5$  with the short inlet pipe, for which the momentum thickness is approximately one-third the value of the long inlet pipe employed for the case of the top row of plots of Fig. 10. In this case, a detectable peak is evident at a relatively low velocity  $U = 60$  ft/s and, correspondingly, the plot of  $Q$ -factor shows a significant peak as well. This low value of onset velocity may be due to the lower total damping of the short-pipe-cavity system, relative to the long-pipe-cavity system. In addition, the initial development of the separated shear layer from the short inlet pipe has an influence on the manner in which large-scale vortices eventually evolve; this difference in evolution might promote a well-defined oscillation at a substantially lower velocity.

In summary, these results of Fig. 10 suggest that larger values of ratio of cavity depth to pipe diameter, i.e., larger  $W^* = W/D$ , promote the onset of flow tones at significantly lower velocities for a pipe-cavity system of constant length. In addition, larger  $W/\theta$  together with a shorter length of the pipe-cavity system promote lower onset velocities.

#### 6.5. Summary of observations of lock-on based on selected criteria

The evaluations of lock-on, presented in Figs. 9a and 10, are representative of those occurring over a broad range of inflow velocity and cavity length, and it is possible to arrive at general observations, which should be applicable to all of the specific cases addressed herein. Two principal criteria for defining lock-on are the focus of our present considerations: (a) a quality  $Q$ -factor of the square of the pressure amplitude as a function of frequency, i.e., the spectrum of the power  $p^2(f)$  of the pressure fluctuation; and (b) the amplitude of the pressure peak  $P$  normalized by the background pressure  $p_{bg}$ , i.e.,  $P/p_{bg}$ . The background pressure  $p_{bg}$  is defined in the top plot of Fig. 9a. It represents the value, obtained by extrapolation, of the magnitude of the background pressure that would exist at the frequency of the peak pressure in the absence of any significant lock-on. In the following, these criteria are defined, then assessed for representative cases.

##### 6.5.1. Definition of lock-on according to quality $Q$ -factor

According to the concept described in Section 6.2, in the absence of any coupling between flow unsteadiness and a resonator, the quality factor  $Q$  of the pressure response spectrum cannot have a value exceeding the  $Q$  of the resonator. In principle, this criterion provides a basis for determining the occurrence of the initial state of lock-on, provided uncertainties in deviations of evaluated  $Q$ -factors are accounted for, as described in Section 2.3. As described therein, values of  $Q$ -factor were determined for the pipe-cavity system subjected to external excitation, as well as to self-excited excitation via throughflow. Despite use of adequate frequency resolution and averaging over a very large number of cycles, significant deviations about a mean value were discernible. In fact, these deviations are evident in virtually all of

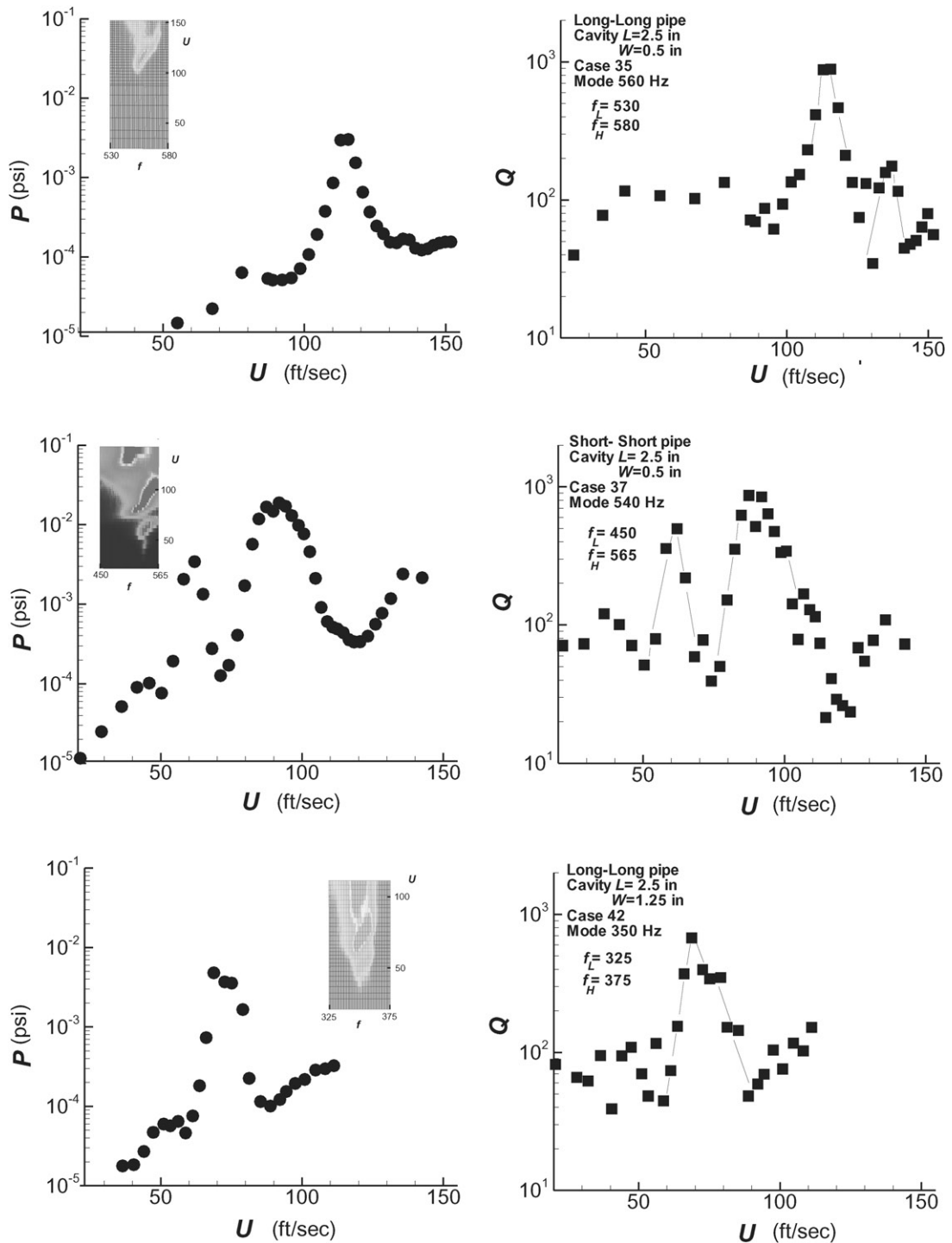


Fig. 10. Onset of initial flow tones. Plots show peak pressure amplitude  $P$  and quality factor  $Q$  as a function of centerline velocity  $U$  for data corresponding to Figs. 4c and d (top set of plots), 5c and d (middle set of plots), and 4a and b (bottom set of plots). Images in the inset of each pressure amplitude plot correspond to a zoomed-in version of a portion of the plan view of the aforementioned sets of plots.

the  $Q$ -factor plots in Figs. 9a and 10. Such deviations are due, at least in part, to the uncertainty of evaluating the  $Q$ -factor.

In the present investigation, the nominal upper limit of the  $Q$ -factor approximately corresponds to the theoretically determined value in absence of mean flow, if one excludes regions where either well-defined peaks or certain “bumps” occur. Values of  $Q$ -factor can extend substantially below this limit due to the effects of mean flow. Inspection of the trends of  $Q$ -factors for the data of Figs. 9a and 10 suggest the occurrence of organized “bumps”. The maximum values of these “bumps” do not exceed a value of  $Q \cong 180$ .

On the basis of these data, values of  $Q$ -factor substantially in excess of  $Q = 180$  are taken to represent occurrence of a locked-on state. In fact, considering the entire range of data displayed in Figs. 9a and 10, the smallest value of  $Q$ -factor of the well-defined peak amplitudes is  $Q = 500$ , and the maximum value is  $Q = 2000$ .

### 6.5.2. Lock-on according to peak pressure amplitude

The variations of peak pressure amplitude  $P$  can be directly compared with the corresponding variations of  $Q$  in each of the plots of Figs. 9a and 10. It is readily apparent that large peaks of  $Q$  essentially correspond to large values of peak pressure  $P$  above the background.

Values of  $(P/p_{bg})_{\max}$  were evaluated for each of the cases of Figs. 9a and 10. The background pressure  $p_{bg}$  is defined in the top plot of Fig. 9a. Parallel with the aforementioned considerations for the  $Q$ -factor, where small-amplitude “bumps” of  $Q$ -factor are discernible, it is possible to consider the corresponding “bumps” of the distributions of peak pressure  $P$  versus velocity  $U$  in Figs. 9a and 10. For all cases considered, the maximum dimensionless amplitude of a “bump” was  $P/p_{bg} \cong 2.0$ .

Consider the well-defined peaks of distributions of amplitude  $P$ , given in Figs. 9a and 10. The values of  $(P/p_{bg})_{\max}$  range from 40 to 100. In parallel with reasoning for the aforementioned  $Q$ -factor criterion, a peak amplitude ratio  $P/p_{bg}$  in excess of 2.0 is taken to be an indication of a pronounced lock-on and, in fact, the smallest value of 40 indicates that this limit is indeed well exceeded.

## 7. Concluding remarks

An overview of the principal findings of the present investigation is provided in this section. Detailed values of parameters and other specifics related to these findings are summarized at the end of each of the preceding sections. In the following, the onset of self-excited oscillations is addressed with respect to the inherent instability of the shear layer past the cavity and its relation to the generation of relatively large-scale modes of flow tone lock-on, the dimensionless frequencies and pressure amplitudes associated with these modes, and the criteria for lock-on.

### 7.1. Transformation from fully turbulent inflow to highly coherent flow tones

A central issue in this investigation is generation of highly coherent flow tones from a fully turbulent inflow. Considerable effort was devoted to the generation of fully turbulent shear flow at the inlet of the cavity, including the case of a fully developed turbulent pipe flow. For appropriate ranges of parameters, highly coherent flow tones emerge. It is hypothesized that the inherent, inviscid instability of the shear layer past the cavity is reinforced by coupling with an acoustic resonant mode of the pipe. This process would then dominate the background turbulence of the inflow. The fact that the inviscid instability of the shear layer plays a clear role is suggested by agreement between dimensionless frequencies of the flow tone and frequencies of instabilities of the shear layer predicted from inviscid theory. This observation suggests that the time-averaged turbulent background flow can serve as the mean flow for the development of the inviscid instability in the shear layer.

### 7.2. Generation and scaling of flow tones in the large-scale mode

Of primary interest in this investigation is generation of flow tones in a large-scale mode, which is defined to occur at relatively long cavity lengths. Its frequency scales with the pipe diameter. This mode occurs for extremes of boundary layer thickness generated at the cavity inlet, thereby reaffirming the scaling based on pipe diameter.

Flow tones in the large-scale mode can be generated in very shallow, long cavities, where the length of the cavity is an order of magnitude larger than its depth, and the cavity depth is as small as one-fourth the pipe diameter. Generally speaking, the peak amplitude of the fluctuating pressure decreases as cavity depth decreases. In the limit, if the cavity depth is shallow, of the order of one-eighth of the pipe diameter, flow tones cannot be generated in the large-scale mode, at least for the range of acoustic damping of the present system. This finding is most likely due to the lack of generation

of a well-defined instability wave or vortex pattern, and the minimal distortion of the trajectory of the acoustic particle velocity near the corners of the cavity, both of which are related to the magnitude of the acoustic power generation.

Scaling of the pressure fluctuations involves two types of dimensionless groups. For sufficiently deep cavities and minimum damping corresponding to the short-pipe system, the dimensionless pressure amplitude of a flow tone, using the inflow dynamic pressure for normalization, is  $p/(\rho U^2/2) \sim 0.6$ ; correspondingly, the pressure amplitude normalized on inflow velocity and the speed of sound can attain values as high as  $p/(\rho U c) \sim 0.04$ . On the other hand, for shallower cavities and relative high damping corresponding to the long-pipe system, flow tones having low amplitudes of  $p/(\rho U^2/2) \sim 0.007$  and  $p/\rho U c \sim 0.0003$  can be generated. For this case, it is hypothesized that a degree of intermittency of the lock-on process may contribute to low-pressure magnitudes, even though the pressure response characteristics are sharp and indicate lock-on. A detailed summary of the concepts and issues related to this type of scaling is given in Section 4.4.

Scaling of the frequencies of the flow tones of the large-scale mode involve, first of all, scaling based on the pipe diameter  $D$ , i.e.,  $fD/U = \text{constant}$ . Remarkable is the fact that this scaling holds for all values of cavity depth  $W$  for which flow tones are generated, even for cavities sufficiently shallow such that large-scale vortex formation is not expected to occur. Apparently, a mechanism for a long wavelength, large-scale mode persists. Moreover, even for the shallowest cavity for which flow tones do not occur, excitation of the pipe modes occurs over a band of preferential frequencies that satisfy the  $fD/U$  scaling. This scaling is described in detail in Section 5.2.

The frequencies of flow tones can also be scaled in accordance with the cavity length, i.e.,  $fL/U = K$ . A variety of scaling correlations have been compared with the present set of data, but no single correlation adequately characterizes the flow tone frequency  $fL/U$  over the wide ranges of parameters addressed herein. Generally speaking, however, the large-scale mode tends to occur at the second mode, or stage,  $n = 2$  defined by these correlations. The results of this type of dimensionless scaling are described in Section 5.1.2.

### 7.3. Nature of locked-on flow tones

Criteria, or indicators, for assessing the occurrence of locked-on flow tones have been addressed and evaluated. The first is the quality  $Q$ -factor of the power spectrum of the pressure fluctuation. After considering a range of representative, locked-on flow states, it is apparent that two types of peaks can occur in variations of  $Q$ -factor with inflow velocity or cavity length. The first are small amplitude, organized “bumps” of the  $Q$ -factor. The maximum value of  $Q$ -factor that occurs for these “bumps” is approximately  $Q = 180$ . The second type of peak in the variation of  $Q$ -factor is much larger; it exceeds by a substantial margin the values of the  $Q$ -factors for the so-called bumps. In fact, these  $Q$ -factors range from  $Q = 500$  to  $2000$ . The fact that these values of  $Q$  are decisively larger than those occurring in the aforementioned band of  $Q$ -factors suggests that they represent robust locked-on flow tones.

The second criterion is the normalized pressure amplitude  $(P/p_{bg})_{\max}$ , in which  $P$  is the amplitude peak of the pressure spectrum and  $p_{bg}$  is the background pressure magnitude that would exist in the absence of flow tone coupling. Analogous observations hold for the ratio  $(P/p_{bg})_{\max}$  for cases where inflow velocity is varied. Small “bumps” of this ratio have a maximum value of  $(P/p_{bg})_{\max} \cong 2.0$ . On the other hand, the onset of pronounced peaks yields values of  $(P/p_{bg})_{\max}$  from 40 to 100. For cases where cavity length is varied, similar bumps and peaks of  $(P/p_{bg})_{\max}$  occur, but their correspondence with the features of the  $Q$ -factor is not as consistent.

## References

- Blake, W.K., 1986. . Mechanics of Flow-Induced Sound and Vibration, Vols. 1 and 2. Academic Press, New York.
- Browand, F.K., Laufer, J., 1975. The role of large-scale structures in the initial development of circular jets. *Turbulence of Liquids* 4, 333–334.
- Bruggeman, J.C., Hirschberg, A., Van Dongen, M.E.H., Wijnands, A.P.J., Gorter, J., 1989. Flow induced pulsations in gas transport systems: analysis of the influence of closed side branches. *ASME Journal of Fluids Engineering* 111, 484–491.
- Bruggeman, J.C., Hirschberg, A., Van Dongen, M.E.H., Wijnands, A.P.J., Gorter, J., 1991. Self-sustained aero-acoustic pulsations in gas transport systems: experimental study of the influence of closed side branches. *Journal of Sound and Vibration* 150, 371–393.
- Cremer, L., Ising, H., 1967/1968. Die selbsterregte schwingungen von orgelpfeifen. *Acustica* 19, 143–153.
- Crighton, D.G., 1992. The jet-edge-tone feedback cycle: linear theory for the operating stages. *Journal of Fluid Dynamics* 234, 361–392.
- Crow, S.C., Champagne, F.H., 1971. Orderly structure in jet turbulence. *Journal of Fluid Mechanics* 48, 547–591.
- Cumpsty, N.S., Whitehead, D.S., 1971. The excitation of acoustic resonances by vortex shedding. *Journal of Sound and Vibration* 18, 353–369.
- Davies, P.O.A.L., 1981. Flow-acoustic coupling in ducts. *Journal of Sound and Vibration* 77, 191–209.

- Davies, P.O.A.L., 1996a. Piston engine intake and exhaust system design. *Journal of Sound and Vibration* 190, 677–712.
- Davies, P.O.A.L., 1996b. Aeroacoustics and time varying systems. *Journal of Sound and Vibration* 190, 345–362.
- Demetz, F.C., Farabee, T.M., 1977. Laminar and turbulent shear flow-induced resonances. AIAA Paper 77-1293.
- Elder, S.A., 1978. Self-excited depth-mode resonance for a wall-mounted cavity in turbulent flow. *Journal of the Acoustical Society of America* 64, 877–890.
- Elder, S.A., Farabee, T.M., Demetz, F.C., 1982. Mechanisms of flow-excited cavity tones at low Mach number. *Journal of the Acoustical Society of America* 72, 532–549.
- Flatau, A., Van Moorham, W.K., 1990. Prediction of vortex shedding responses in segmented solid rocket motors. AIAA Paper 90-2073.
- Fletcher, N.H., 1979. Air flow and sound generation in musical wind instruments. *Annual Review of Fluid Mechanics* 11, 123–146.
- Hourigan, K., Welsh, M.C., Thompson, M.C., Stokes, A.N., 1990. Aerodynamic sources of acoustic resonance in a duct with baffles. *Journal of Fluids and Structures* 4, 345–370.
- Howe, M.S., 1975. Contributions to the theory of aerodynamic sound with applications to excess jet noise and the theory of the flute. *Journal of Fluid Mechanics* 71, 625–673.
- Howe, M.S., 1980. The dissipation of sound at an edge. *Journal of Sound and Vibration* 70, 407–411.
- Howe, M.S., 1997. Edge, cavity and aperture tones at very low Mach numbers. *Journal of Fluid Mechanics* 330, 61–84.
- Howe, M.S., 1998. *Acoustics of Fluid-Structure Interaction*. Cambridge University Press, Cambridge.
- Kline, S.J., McClintock, F.A., 1953. Describing uncertainties in single sample experiments. *ASME Mechanical Engineering* 75, 3–8.
- Knisely, C., Rockwell, D., 1982. Self-sustained low-frequency components in an impinging shear layer. *Journal of Fluid Mechanics* 116, 157–186.
- Kriesels, P.C., Peters, M.C.A.M., Hirschberg, A., Wijnands, A.P.J., Iafrati, A., Riccardi, G., Piva, R., Bruggemann, J.-C., 1995. High amplitude vortex-induced pulsations in a gas transport system. *Journal of Sound and Vibration* 184, 343–368.
- Lau, J.C., Fisher, M.J., Fuchs, H.V., 1972. The intrinsic structure of turbulent jets. *Journal of Sound and Vibration* 22, 379–406.
- Naudascher, E., Rockwell, D., 1994. *Flow-Induced Vibrations: An Engineering Guide*. Balkema Press, Rotterdam.
- Nelson, P.A., Halliwell, N.A., Doak, P.E., 1981. Fluid dynamics of a flow excited resonance. Part I: experiment. *Journal of Sound and Vibration* 78, 15–38.
- Nelson, P.A., Halliwell, N., Doak, P.E., 1983. Fluid dynamics of a flow excited resonance. Part II: Flow acoustic interaction. The dissipation of sound at an edge. *Journal of Sound and Vibration* 91, 375–402.
- Newland, D.E., 1993. *An Introduction to Random Vibrations, Spectral and Wavelet Analysis*, 3rd Edition. Prentice-Hall, Reason Education, Essex, UK.
- Nosseir, N.S., Ho, C.-M., 1982. Dynamics of an impinging jet. Part 2. The noise generation. *Journal of Fluid Mechanics* 116, 379–391.
- Parker, R., 1966. Resonance effects in wake shedding from parallel plates: some experimental observations. *Journal of Sound and Vibration* 4, 62–72.
- Peters, M.C.A.M., 1993. Aeroacoustic sources and internal flows. Ph.D. Dissertation, Technical University of Eindhoven.
- Pfizenmaier, E., 1973. On the instability of a sound influenced free jet. E.S.R.O. Technical Transl. 122 (Transl. of DFVLR Berlin Rep. DLR-FB 73-69).
- Pollack, M.L., 1980. Flow-induced tones in side-branch pipe resonators. *Journal of the Acoustical Society of America* 7, 1153–1156.
- Powell, A., 1961. On the edgetone. *Journal of the Acoustical Society of America* 33, 395–409.
- Powell, A., 1964. Theory of vortex sound. *Journal of the Acoustical Society of America* 36, 177–195.
- Rockwell, D., 1983. Oscillations of impinging shear layers. Invited Lecture, 20th Aerospace Sciences Meeting of AIAA, Orlando, FL, January 1981; AIAA Paper 81-0047; also see AIAA Journal 21, 645–664.
- Rockwell, D., 1998. Vortex-body interactions. Invited contribution to *Annual Review of Fluid Mechanics* 30, 199–229.
- Rockwell, D., Karadogan, H., 1982. Oscillations of an impinging turbulent jet: coherence characterization via conditional sampling. *Journal of Sound and Vibration* 83, 111–124.
- Rockwell, D., Karadogan, H., 1983. Toward attenuation of self-sustained oscillations of a turbulent jet through a cavity. *ASME Journal of Fluids Engineering* 105, 335–340.
- Rockwell, D., Naudascher, E., 1978. Review—self-sustaining oscillations of flow past cavities. *ASME Journal of Fluids Engineering* 100, 152–165.
- Rockwell, D., Naudascher, E., 1979. Self-sustained oscillations of impinging free-shear layers. *Annual Review of Fluid Mechanics* 11, 67–94.
- Rockwell, D., Schachenmann, A., 1980. A quasi-standing wave phenomenon due to oscillating internal flow. *ASME Journal of Fluids Engineering* 102, 70–77.
- Rockwell, D., Schachenmann, A., 1982. Self-generation of organized waves in an impinging turbulent jet at low mach numbers. *Journal of Fluid Mechanics* 117, 425–441.
- Rockwell, D., Schachenmann, A., 1983. The organized shear layer due to oscillations of a turbulent jet through an axisymmetric cavity. *Journal of Sound and Vibration* 87, 371–382.

- Rossiter, J.E., 1962. The effect of cavities on the buffeting of aircraft. Royal Aircraft Establishment (UK) Technical Memorandum 754.
- Rossiter, J.E., 1964. Wind tunnel experiments on the flow over rectangular cavities at subsonic and transonic speeds. Reports and Memoranda No. 3438, October.
- Stoneman, S.A.T., Hourigan, K., Stokes, A.N., Welsh, M.E., 1988. Resonant sound caused by flow past two plates in tandem in a duct. *Journal of Fluid Mechanics* 192, 455–484.
- Stoubos, A.K., Benocci, C., Palli, E., Stoubos, G.K., Olivari, D., 1999. Aerodynamically generated acoustic resonance in a pipe with annular flow restrictors. *Journal of Fluids and Structures* 13, 755–778.
- Wilson, T.A., Beavers, G.S., Decoster, M.A., Holger, D.K., Regenfuss, M.D., 1971. Experiments on the fluid mechanics of whistling. *Journal of the Acoustical Society of America* 50, 366–372.
- Ziada, S., Bühlmann, E.T., 1992. Self-excited resonances of two-side-branches in close proximity. *Journal of Fluids and Structures* 6, 583–601.
- Ziada, S., Shine, S., 1999. Strouhal numbers of flow-excited acoustic resonance of closed side branches. *Journal of Fluids and Structures* 13, 127–142.